PAPER • OPEN ACCESS

Global fluid simulation of plasma turbulence in stellarators with the GBS code

Global fluid simulation of plasma turbulence in stellarators with the GBS code

A.J. Coelho[*] , **J. Loizu, P. Ricci and Z. Tecchiolli**

Ecole Polytechnique Fédérale de Lausanne (EPFL), Swiss Plasma Center (SPC), CH-1015 Lausanne, Switzerland

E-mail: antonio.coelho@epfl.ch

CrossMark

Abstract

The implementation of three-dimensional magnetic fields, such as the ones of stellarators, in the GBS code (Ricci *et al* 2012 *Plasma Phys. Control. Fusion* **54** 124047; Giacomin *et al* 2022 *J. Comput. Phys.* **464** 111294) is presented, and simulation results are discussed. The geometrical operators appearing in the drif-reduced Braginskii equations evolved by GBS are expanded considering the typical parameter ordering of stellarator configurations. It turns out that most of the operators have a similar structure as the one implemented in the tokamak axisymmetric version of the code. In particular, the perpendicular laplacian only acts on the poloidal plane, which avoids the need of a three-dimensional solver for the electrostatic potential. The simulation of an island divertor stellarator is then presented, showing the derivation of the magnetic equilibrium in detail and extending the results in (Coelho *et al* 2022 *Nucl. Fusion* **62** 074004). Although the island magnetic field-lines divert the plasma towards the strike points of the walls, the islands do not seem to have a significant impact on the turbulence properties. The dominant mode, identified as interchange-driven, is field-aligned and breaks the stellarator toroidal symmetry. The radial and poloidal extensions of the mode are of the same order, in contrast to typical tokamak simulations. This has consequences on the poloidal dependence of turbulent transport.

Keywords: stellarator, island divertor, turbulence, GBS, global fluid simulations

(Some figures may appear in colour only in the online journal)

1. Introduction

As stellarators assume an increasing interest as a viable alternative to the tokamak [1, 2], the importance of improving the predictive capabilities of plasma turbulence simulations in three-dimensional magnetic fields grows. Significant effort is devoted to extend gyrokinetic codes to non-axisymmetric magnetic fields, namely GENE-3D [3], XGC-S [4], Stella [5] and EUTERPE [6], with simulations carried out on W7-X and LHD equilibria [7, 8]. Fluid codes, which can properly simulate high-collisional plasmas such as the ones found in the boundary region of fusion devices, are also being extended to non-axisymmetric magnetic field geometries [9, 10]. Our letter in [9] reports on the first global flux-driven fluid simulation of a stellarator, which was performed by using the GBS code and considering an island divertor geometry [9]. The simulation results show important differences with respect to tokamak simulations, namely the fact that turbulent transport is dominated by a coherent mode with low poloidal mode number, where the structures are such that their extensions in the

---

[*] Author to whom any correspondence should be addressed.

radial and poloidal directions are similar. Although such level of coherency and size of the structures is not usual in tokamaks, in stellarators such as TJ-K, a large coherent mode with low poloidal mode number is observed (usually $m = 3$ or $m = 4$ in hydrogen and helium discharges) [11], a feature that GBS simulations of TJ-K were able to retrieve [12].

In our initial work reporting a simulation of a stellarator with an island divertor [9], the drive of the dominant mode is identified as a curvature-driven mode with a ballooning nature. The investigation of the nature of the mode is achieved by means of a simplified linear theory. The surprising result that the non-linear turbulent flux is larger on the high-field side (HFS) than on the low-field side (LFS) is not explained.

In this paper we extend the results presented in [9]. We present a detailed description of the model used to perform stellarator simulations and its implementation in GBS. We analyse in more detail the simulation results and, in particular, the nature of the mode dominating the transport, and develop a more complete linear theory that takes into account the stellarator geometry, which is able to explain the peaking of the turbulent transport at the HFS.

The present paper is organized as follows. Section 2 describes the extension of the GBS code to 3D magnetic fields. In section 3, we present the Dommaschk potentials which are used to generate stellarator vacuum fields. In section 4, results of an island divertor stellarator simulation is presented. Finally, our conclusions are drawn in section 5.

2. Extension of the GBS code to 3D configurations

GBS [13–15] is a three-dimensional, global, two-fluid, flux-driven code that solves the drift-reduced Braginskii equations [16], valid in the high-collisionality regime that often characterizes the plasma boundary of magnetic fusion devices, as well as the core of low-temperature devices such as the TORPEX basic plasma physics experiment [17] or the TJ-K stellarator [12]. GBS evolves all quantities in time, without separation between equilibrium and fluctuating components. In the version of GBS with non-axisymmetric magnetic fields, the electrostatic limit is taken, the Boussinesq approximation is employed [13] and the gyroviscous terms, as well as the coupling to the neutral dynamics, are neglected, although these are implemented in the most recent version of the GBS code for tokamak simulations [14]. Within these approximations, the drift-reduced model evolved by GBS is:

$$\frac{\partial n}{\partial t} = -\frac{\rho_*^{-1}}{B} [\Phi, n] - \nabla_\parallel \left(n V_{\parallel e} \right) + \frac{2}{B} \left[C(p_e) - nC(\Phi) \right] + D_n \nabla_\perp^2 n + D_n^\parallel \nabla_\parallel^2 n + \mathcal{S}_n \tag{1}$$

$$\frac{\partial T_e}{\partial t} = -\frac{\rho_*^{-1}}{B} [\Phi, T_e] - V_{\parallel e} \nabla_\parallel T_e + \frac{4T_e}{3B} \left[\frac{C(p_e)}{n} + \frac{5}{2} C(T_e) - C(\Phi) \right] + \frac{2T_e}{3n} \left[0.71 \nabla_\parallel j_\parallel - n \nabla_\parallel V_{\parallel e} \right] + D_{T_e} \nabla_\perp^2 T_e + \chi_{\parallel e} \nabla_\parallel^2 T_e + \mathcal{S}_{T_e} \tag{2}$$

$$\frac{\partial T_i}{\partial t} = -\frac{\rho_*^{-1}}{B} [\Phi, T_i] - V_{\parallel i} \nabla_\parallel T_i + \frac{4T_i}{3B} \left[\frac{C(p_e)}{n} - \frac{5}{2} \tau C(T_i) - C(\Phi) \right] + \frac{2T_i}{3n} \left[\nabla_\parallel j_\parallel - n \nabla_\parallel V_{\parallel i} \right] + D_{T_i} \nabla_\perp^2 T_i + \chi_{\parallel i} \nabla_\parallel^2 T_i + \mathcal{S}_{T_i} \tag{3}$$

$$\frac{\partial V_{\parallel e}}{\partial t} = -\frac{\rho_*^{-1}}{B} \left[\Phi, V_{\parallel e} \right] - V_{\parallel e} \nabla_\parallel V_{\parallel e} + \frac{m_i}{m_e} \left[\nu j_\parallel + \nabla_\parallel \Phi - \frac{\nabla_\parallel p_e}{n} - 0.71 \nabla_\parallel T_e \right] + \eta_{0e} \nabla_\parallel^2 V_{\parallel e} + D_{V_{\parallel e}} \nabla_\perp^2 V_{\parallel e} \tag{4}$$

$$\frac{\partial V_{\parallel i}}{\partial t} = -\frac{\rho_*^{-1}}{B} \left[\Phi, V_{\parallel i} \right] - V_{\parallel i} \nabla_\parallel V_{\parallel i} - \frac{1}{n} \nabla_\parallel \left(p_e + \tau p_i \right) + \eta_{0i} \nabla_\parallel^2 V_{\parallel i} + D_{V_{\parallel i}} \nabla_\perp^2 V_{\parallel i} \tag{5}$$

$$\frac{\partial \omega}{\partial t} = -\frac{\rho_*^{-1}}{B} [\Phi, \omega] - V_{\parallel i} \nabla_\parallel \omega + \frac{B^2}{n} \nabla_\parallel j_\parallel + \frac{2B}{n} C(p_e + \tau p_i) + D_\omega \nabla_\perp^2 \omega + D_\omega^\parallel \nabla_\parallel^2 \omega \tag{6}$$

which are closed by

$$\nabla_\perp^2 \Phi = \omega - \tau \nabla_\perp^2 T_i. \tag{7}$$

In equations (1)–(7), and in the rest of the paper, density n, electron temperature T_e and ion temperature T_i are normalized to the reference values n_0, T_{e0} and T_{i0}, respectively; electron parallel velocity $V_{\parallel e}$ and ion parallel velocity $V_{\parallel i}$ are both normalized to the sound speed $c_{s0} = \sqrt{T_{e0}/m_i}$; vorticity ω and the electrostatic potential Φ are normalized to $T_{e0}/(e\rho_{s0}^2)$ and T_{e0}/e; time is normalized to R_0/c_{s0}, where R_0 is the machine major radius; perpendicular and parallel lengths are normalized to the ion sound Larmor radius, $\rho_{s0} = \sqrt{T_{e0} m_i}/(e B_0)$, and R_0, respectively; the normalized parallel current is $j_\parallel = n(V_{\parallel i} - V_{\parallel e})$ and the magnetic field B is normalized to the magnitude of the field on axis, B_0.

The dimensionless parameters appearing in equations (1)–(7) are the normalized ion sound Larmor radius $\rho_* = \rho_{s0}/R_0$, the normalized electron and ion parallel heat diffusivities, $\chi_{\parallel e}$ and $\chi_{\parallel i}$, considered constants here, the ion to electron temperature ratio $\tau = T_{i0}/T_{e0}$, the normalized electron and ion viscosities, η_{0e} and η_{0i}, which we assume to have constant values, and the normalized Spitzer resistivity, $\nu = \nu_0 T_e^{-3/2}$, with

$$\nu_0 = \frac{4\sqrt{2\pi}}{5.88} \frac{e^4}{(4\pi\varepsilon_0)^2} \frac{\sqrt{m_e} R_0 n_0 \lambda}{m_i c_{s0} T_{e0}^{3/2}}, \tag{8}$$

where λ denotes the Coulomb logarithm [18]. Small numerical diffusion terms such as $D_n \nabla_\perp^2 n$ and $D_n^\parallel \nabla_\parallel^2 n$ (and similar for the other fields) are introduced to improve the numerical stability of the simulations (the simulation results show that they

Table 1. Boundary conditions applied at the top, bottom, inner and outer domain boundaries. The derivative $\partial_s = \boldsymbol{s} \cdot \boldsymbol{\nabla}$ is along the direction normal to the surface, $\boldsymbol{s}$. The upper signs apply if the magnetic field is directed towards the wall, while the lower signs apply in the opposite case. It is defined $F_T = \sqrt{1 + \tau T_i/T_e}$ and $\Lambda = 3$ [21].

	Top and bottom walls	Inner and outer walls
$V_{\parallel e}$	$V_{\parallel e} = \pm\sqrt{T_e}\exp\left(\Lambda - \Phi/T_e\right)$	$\partial_s V_{\parallel e} = 0$
$V_{\parallel i}$	$V_{\parallel i} = \pm\sqrt{T_e}F_T$	$\partial_s V_{\parallel i} = 0$
ω	$\omega = 0$	$\omega = 0$
n	$\partial_s n = 0$	$\partial_s n = 0$
Φ	$\partial_s \Phi = \pm\frac{\sqrt{T_e}}{F_T}\partial_s v_{\parallel i}$	$\Phi = \Lambda T_e$
T_e, T_i	$\partial_s T_e = \partial_s T_i = 0$	$\partial_s T_e = \partial_s T_i = 0$

have a negligible effect on turbulence since they lead to significantly lower perpendicular transport than turbulence). The terms $\mathcal{S}_n$, $\mathcal{S}_{T_e}$ and $\mathcal{S}_{T_i}$ denote the density, electron temperature and ion temperature sources, respectively. Magnetic pre-sheath boundary conditions, described in [19, 20], are applied to all quantities at the top and bottom boundaries of the simulation domain. For the stellarator simulations presented here, the density and vorticity at the boundary satisfy, respectively, $\partial_s n = 0$ and $\omega = 0$, where $\partial_s = \boldsymbol{s} \cdot \boldsymbol{\nabla}$ is the derivative along the direction normal to the wall, $\boldsymbol{s}$. This choice is due to stability reasons. A summary of the applied boundary conditions is given in table 1.

The GBS simulation domain is a torus of radius R_0 with a rectangular cross-section of size $L_R \times L_Z$. The physical model in equations (1)–(7) is discretized using a regular cylindrical grid (R, ϕ, Z), with R the radial coordinate, ϕ the toroidal angle and Z the vertical coordinate. Equations (1)–(6) are advanced in time using an explicit Runge–Kutta fourth-order scheme, while spatial derivatives are computed with a fourth-order finite difference scheme.

The normalized geometrical operators appearing in equations (1)–(7) are the parallel gradient $\nabla_\parallel u = \boldsymbol{b} \cdot \boldsymbol{\nabla} u$, the Poisson brackets, $[\Phi, u] = \boldsymbol{b} \cdot [\boldsymbol{\nabla}\Phi \times \boldsymbol{\nabla} u]$, the curvature operator, $C(u) = (B/2)\left[\boldsymbol{\nabla} \times (\boldsymbol{b}/B)\right] \cdot \boldsymbol{\nabla} u$, the parallel Laplacian, $\nabla_\parallel^2 u = \boldsymbol{b} \cdot \boldsymbol{\nabla}(\boldsymbol{b} \cdot \boldsymbol{\nabla} u)$, and the perpendicular Laplacian $\nabla_\perp^2 u = \boldsymbol{\nabla} \cdot [(\boldsymbol{b} \times \boldsymbol{\nabla} u) \times \boldsymbol{b}]$. For their numerical implementation in three-dimensional magnetic field configurations, we expand these operators in the following small parameters: $\delta = B_R/B \sim B_Z/B$, where B_R and B_Z are the radial and vertical components of the magnetic field; the normalized mirror ratio, $\Delta = (B_{\max} - B_{\min})/\overline{B}$, where $\overline{B}$ is the toroidally averaged value of B along the magnetic axis and $(B_{\max} - B_{\min})$ is the toroidal ripple amplitude; and the ratio between perpendicular and parallel turbulence length scales, $\sigma = l_\perp/l_\parallel$. We then retain only the leading order terms in these expansion parameters as shown in appendix A. For the stellarator configuration considered in this work $\delta \sim 0.1$, $\Delta \lesssim 0.1$ and *a posteriori* we verify that $\sigma \sim 0.01$, confirming the validity of our expansion. In the particular case of a vacuum field, the operators are, after expansion,

$$\nabla_\parallel u = \frac{B_R}{B}\rho_*^{-1}\frac{\partial u}{\partial R} + \texttt{sign}\left(\frac{B_\phi}{B}\right)\frac{R_0}{R}\frac{\partial u}{\partial \phi} + \frac{B_Z}{B}\rho_*^{-1}\frac{\partial u}{\partial Z} \quad (9)$$

$$C(u) = R_0\left[\frac{1}{B}\frac{\partial B_\phi}{\partial Z}\right]\frac{\partial u}{\partial R} + R_0\left[-\frac{1}{B}\frac{\partial B_\phi}{\partial R}\right]\frac{\partial u}{\partial Z} \quad (10)$$

$$[\Phi, u] = \texttt{sign}\left(\frac{B_\phi}{B}\right)\frac{\partial \Phi}{\partial Z}\frac{\partial u}{\partial R} - \texttt{sign}\left(\frac{B_\phi}{B}\right)\frac{\partial \Phi}{\partial R}\frac{\partial u}{\partial Z} \quad (11)$$

$$\nabla_\perp^2 u = \frac{\partial^2 u}{\partial R^2} + \frac{\partial^2 u}{\partial Z^2} \quad (12)$$

$$\begin{aligned}
\nabla_\parallel^2 u = {} & R_0\left[\frac{B_R}{B}\frac{1}{B}\frac{\partial B_R}{\partial R} + \texttt{sign}\left(\frac{B_\phi}{B}\right)\frac{1}{R}\frac{1}{B}\frac{\partial B_R}{\partial \phi} + \frac{B_Z}{B}\frac{1}{B}\frac{\partial B_R}{\partial Z}\right]\rho_*^{-1}\frac{\partial u}{\partial R} \\
& + R_0\left[\frac{B_R}{B}\frac{1}{B}\frac{\partial B_Z}{\partial R} + \texttt{sign}\left(\frac{B_\phi}{B}\right)\frac{1}{R}\frac{1}{B}\frac{\partial B_Z}{\partial \phi} + \frac{B_Z}{B}\frac{1}{B}\frac{\partial B_Z}{\partial Z}\right]\rho_*^{-1}\frac{\partial u}{\partial Z} \\
& + \left(\frac{B_R}{B}\right)^2(\rho_*^{-1})^2\frac{\partial^2 u}{\partial R^2} + \left(\frac{R_0}{R}\right)^2\frac{\partial^2 u}{\partial \phi^2} + \left(\frac{B_Z}{B}\right)^2(\rho_*^{-1})^2\frac{\partial^2 u}{\partial Z^2} \\
& + 2\frac{B_R}{B}\texttt{sign}\left(\frac{B_\phi}{B}\right)\frac{R_0}{R}\rho_*^{-1}\frac{\partial^2 u}{\partial R\partial \phi} + 2\frac{B_R}{B}\frac{B_Z}{B}(\rho_*^{-1})^2\frac{\partial^2 u}{\partial R\partial Z} \\
& + 2\texttt{sign}\left(\frac{B_\phi}{B}\right)\frac{B_Z}{B}\frac{R_0}{R}\rho_*^{-1}\frac{\partial^2 u}{\partial \phi\partial Z}.
\end{aligned} \quad (13)$$

Since the geometrical operators (9)–(13) have the same structure as the ones implemented in the axisymmetric version of GBS [14], their implementation does not require major changes in the structure of the code thanks to the use of a non field-aligned spatial discretization algorithm [22, 23]. In fact, as in the previous versions of GBS, an Arakawa scheme is applied to implement the Poisson brackets [23], and the same solver used to invert equation (7) can be considered, since the perpendicular Laplacian only acts on the RZ-plane (to lowest order in the expansion parameters δ, Δ and σ).

3. Stellarator vacuum magnetic field based on the Dommaschk potentials

The stellarator vacuum magnetic field generated by any set of external coils can be described using appropriate basis functions that completely span the space of field solutions. A vacuum field obeys $\nabla \times \mathbf{B} = 0$, meaning that $\mathbf{B} = \nabla V$, where V is denoted as the magnetic potential. Since $\nabla \cdot \mathbf{B} = 0$, V satisfies a Laplace equation, $\nabla^2 V = 0$. There are several sets of analytical functions that solve Laplace's equation in a torus, namely, toroidal field harmonics, spherical harmonics or the Vuillemin-Gourdon set [24, 25]. A set of functions that has advantages over the other sets is the one commonly known as Dommaschk potentials [26–28], which are given in cylindrical coordinates by

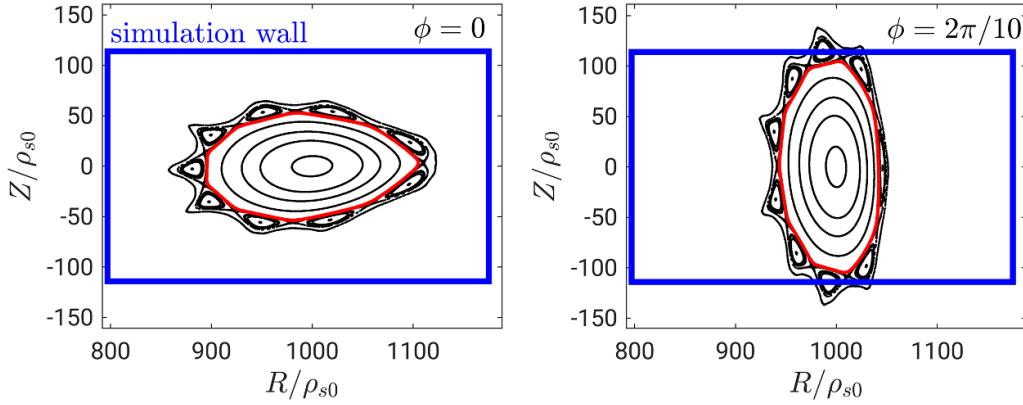$$V(R, \phi, Z) = \phi + \sum_{m,l} V_{m,l}(R, \phi, Z), \quad (14)$$

Figure 1. Poincaré plot of the Dommaschk configuration $b_{5,2} = c_{5,2} = 1.5$, $b_{5,4} = 10$, $a_{5,9} = -d_{5,9} = -7.5 \times 10^9$ on two poloidal planes at different toroidal angles. The boundary of the simulation domain is represented in blue and the LCFS in red.

where

$$
\begin{aligned}
V_{m,l} = &\left[a_{m,l}\cos\left(m\phi\right) + b_{m,l}\sin\left(m\phi\right)\right] D_{m,l}\left(R,Z\right) \\
&+ \left[c_{m,l}\cos\left(m\phi\right) + d_{m,l}\sin\left(m\phi\right)\right] N_{m,l-1}\left(R,Z\right). \quad (15)
\end{aligned}
$$

$a_{m,l}$, $b_{m,l}$, $c_{m,l}$ and $d_{m,l}$ are free real constants and $D_{m,l}$, $N_{m,l}$ are explicit functions given in [26]. The first term on the right-hand side of equation (14) gives the $1/R$ dependence of the toroidal component of the magnetic field. The Dommaschk potentials are advantageous over others sets of solutions because the $V_{m,l}$ functions consist of simple algebraic expressions (powers, logarithms, sines and cosines) whose numerical evaluation is computationally convenient. Furthermore, the indices m and l correspond, respectively, to the toroidal and poloidal periodicities of $V_{m,l}$, a property that for example the spherical harmonics lack [26]. As a consequence, if the field is generated with potentials restricted to $m = kN_{\mathrm{fp}}$ and $k \in \mathbb{N}$, then the stellarator has field period N_{fp}. In addition, stellarator symmetry [29] requires $a_{m,l} = d_{m,l} = 0$ for even l, and $b_{m,l} = c_{m,l} = 0$ for odd l.

We have constructed a five-field period ($N_{\mathrm{fp}} = 5$) stellarator-symmetric configuration with a 5/9 chain of islands surrounding a closed flux surface region by taking $b_{5,2} = c_{5,2} = 1.5$, $b_{5,4} = 10$, $a_{5,9} = -d_{5,9} = -7.5 \times 10^9$, and imposing all other coefficients to vanish. Figure 1 shows the corresponding Poincaré plot of the magnetic field at different toroidal angles. The potential $V_{5,9}$ is added in order to control the width of the 5/9 islands. In fact, this potential resonates with the 5/9 rational surface and can be used to increase the size of the islands. If $V_{5,9}$ becomes too large, a chaotic region is generated due to the overlap of different island chains. This is shown in figure 2 where the Poincaré sections with $a_{5,9} = -d_{5,9} = -15 \times 10^9$ reveal a chaotic region outside the last closed flux surface (LCFS) instead of an island chain.

The rotational transform ι is entirely provided by the rotation of the flux surfaces since no torsion is present in the configuration considered here (the magnetic axis lies on a plane) nor current. We can estimate the expected rotational transform on axis, ι_0, from the elongation of the ellipses [30, 31], that is $\iota_0 = (N_{\mathrm{fp}}/2)(r_{\max} - r_{\min})^2/(r_{\min}^2 +$

$r_{\max}^2) \approx 0.5$, where $r_{\max}$ and $r_{\min}$ are the ellipses major and minor radius, which is in very good agreement with the ι evaluated numerically by field-line tracing and depicted in figure 3. The ι profile flattens at $\iota = 5/9 \approx 0.555$, where the island chain is present. We note that the magnetic shear is very small.

The amplitude of **B** varies approximately as $1/R$, as in a tokamak. Therefore, a LFS and a HFS can be identified, similarly to tokamaks. This can be seen in figure 4 where we show $|\mathbf{B}|$ on the LCFS. In fact, $|\mathbf{B}|$ peaks at $\theta = \pi$ and is minimized around $\theta = 0$, where θ is the polar angle defined with respect to the magnetic axis that rotates anti-clockwise, with the outboard midplane corresponding to $\theta = 0$ and the inboard midplane to $\theta = \pi$.

The height and width of the rectangular computational domain cross-section can be taylored such that the magnetic field of the islands intercept the top and bottom of the simulation box, as shown in figure 5, emulating an *island divertor* stellarator. In such a configuration, the LCFS *is not* in contact with the wall. Heat and particles outflowing from the core reach the island region and are transported along the magnetic field of the islands, eventually striking the top and bottom walls at specific toroidal locations. The strike points of the island magnetic field lines at the top of the simulation box are indicated in figure 6(a). A similar structure is found on the bottom part of the box. On the other hand, the Dommaschk configuration without islands, shown in figure 2, yields a *limited* stellarator. In such configuration, the LCFS *is* in contact with the wall.

It is noteworthy to mention the similarities between our island divertor stellarator model and W7-X. Our configuration leads to large connection lengths in the island region ($L_c \sim 100R_0$) as seen in figure 5(right), similarly to W7-X where connection lengths of the order of hundreds of meters are found in the edge [32]. In addition, in W7-X the magnetic shear is also small. Finally, a chain of islands surrounds the closed flux surface region in W7-X and the plasma is evacuated through the magnetic islands that strike non-axisymmetric divertor targets, although in our case the divertor targets are axisymmetric.
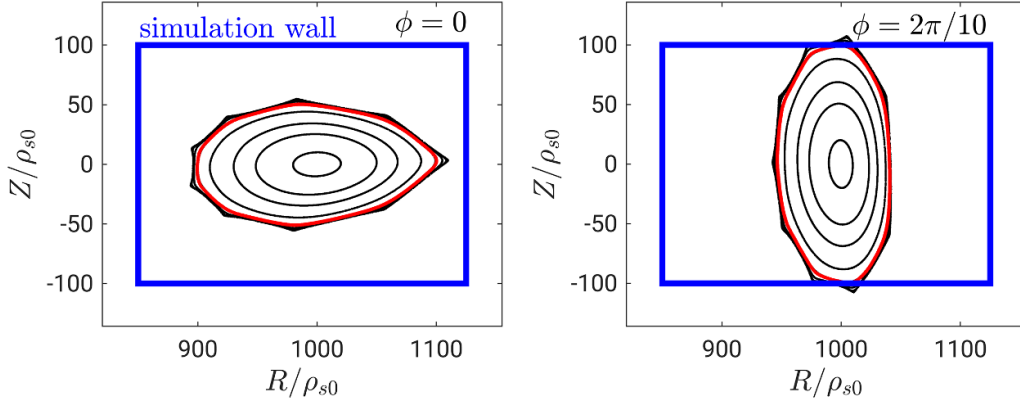
Figure 2. Poincaré plot of the Dommaschk configuration $b_{5,2} = c_{5,2} = 1.5$, $b_{5,4} = 10$, $a_{5,9} = -d_{5,9} = -15 \times 10^9$ on two poloidal planes at different toroidal angles. The boundary of the simulation domain is represented in blue and the LCFS in red.
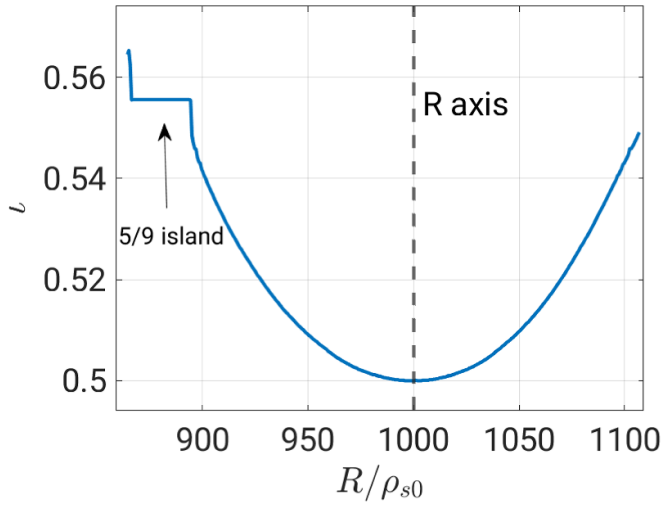

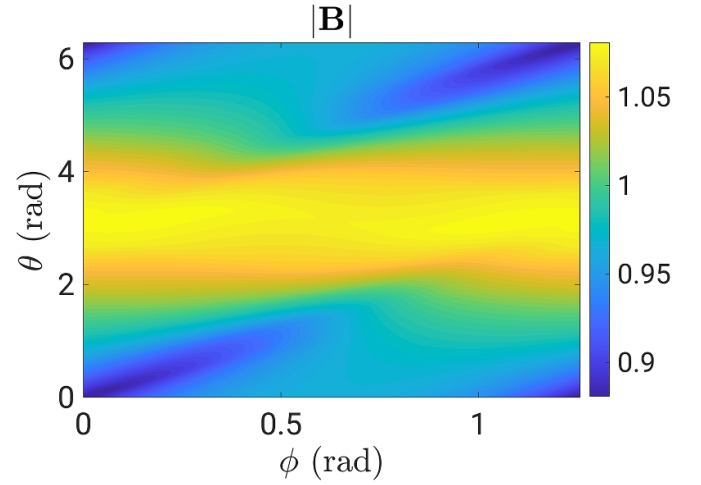**Figure 3.** Rotational transform along R at $Z = 0$ and $\phi = 0$.

Figure 4. Amplitude of the magnetic field on the LCFS as a function of the polar angle θ defined with respect to the magnetic axis and the toroidal angle ϕ. Only one field period is displayed.

4. Results

4.1. Simulation parameters and convergence

We use the following parameters for the simulations discussed in this paper: $\rho_*^{-1} = 1000$, $\nu_0 = 0.1$, $\tau = 1$, $\chi_{\|e,i} = \eta_{0e,i} = 1.0$, $D_n = D_{T_e} = D_{T_i} = D_{V_{\|e}} = D_{V_{\|i}} = D_\omega = 10$, $D_n^\| = D_\omega^\| = 1$, $L_R = 380\rho_{s0}$, $L_Z = 230\rho_{s0}$, a grid resolution of $N_R \times N_Z \times N_\phi = 200 \times 120 \times 200$ points and a time-step of $2.9 \times 10^{-6} R_0/c_{s0}$. The convergence of the simulation is assessed by performing a simulation with grid $N_R \times N_Z \times N_\phi = 250 \times 150 \times 200$ and a second one with grid $N_R \times N_Z \times N_\phi = 250 \times 150 \times 250$, which is at the limit of our computational capabilities. In both cases the dynamics of the simulation is similar to the one presented here. The sources for density and temperature, $\mathcal{S}_n = \mathcal{S}_{T_e} = \mathcal{S}_{T_i}$, are localized around a magnetic surface near the LCFS, as shown in figure 7, mimicking the ionization of recycled neutrals. We have performed simulations with *forward* and *reversed* magnetic field by reversing the total **B**, i.e. the sign of equation (14). We denote these two cases with $B_\phi > 0$ and $B_\phi < 0$, respectively. In what follows,

if not mentioned, we are referring to the simulation with *forward* magnetic field ($B_\phi > 0$), which corresponds to an anti-clockwise toroidal magnetic field seen from above.

4.2. Quasi-steady state and balance between particle sources and fluxes

The simulations are started from a noisy initial state and, after a transient, reach a quasi-steady state where sources, parallel and perpendicular transport and, ultimately, losses at the vessel balance each other. If we volume-integrate equation (1) we obtain

$$
\begin{aligned}
&\frac{\partial}{\partial t} \int n \mathrm{d}V + \int \left[\frac{\rho_*^{-1}}{B} [\Phi, n] + \frac{2}{B} n C(\Phi) \right] \mathrm{d}V \\
&\quad + \int \frac{-2}{B} C(p_e) \mathrm{d}V + \int \nabla_\| (n V_{\|e}) \mathrm{d}V \\
&\quad - \int D_n \nabla_\perp^2 n \mathrm{d}V - \int D_n^\| \nabla_\|^2 n \mathrm{d}V = \int \mathcal{S}_n \mathrm{d}V.
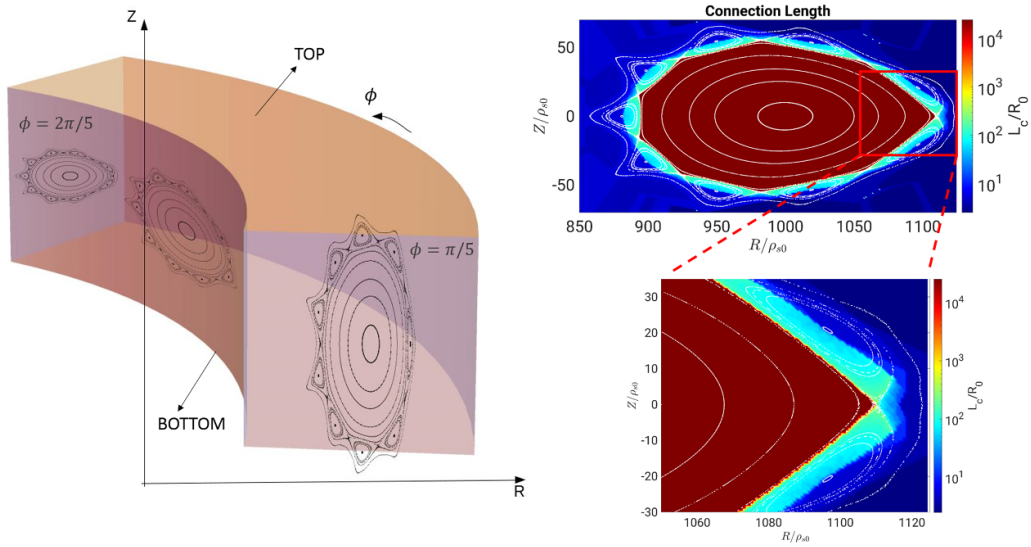\end{aligned}
\tag{16}
$$

Figure 5. (Left) 1/10 of the simulation box. Note how the height and width of the cross-section of the simulation domain are adjusted to create an island divertor stellarator. (Right) Connection length of the field lines normalized to the major radius, L_c/R_0.
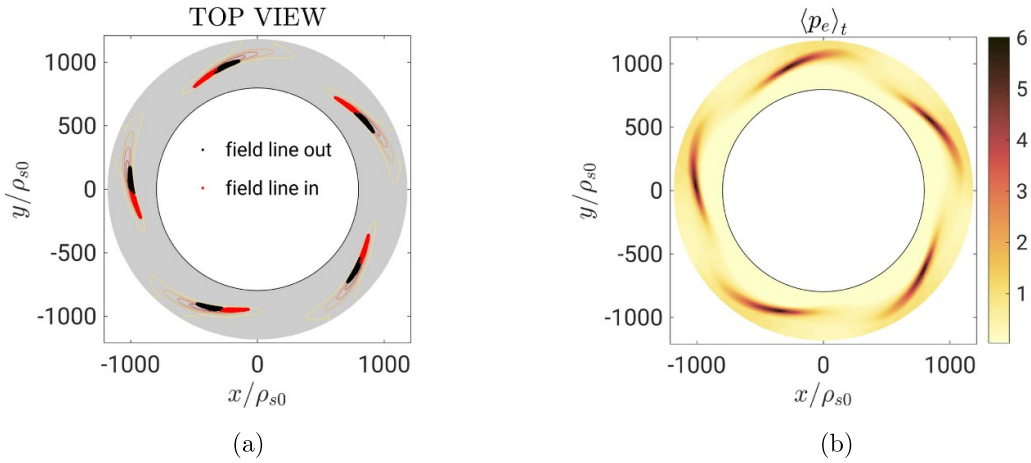

Figure 6. (*a*) Top view of the simulation box. Black dots correspond to field-lines of the island chain leaving the box ($B_Z > 0$) and red dots to field-lines entering ($B_Z < 0$). The contours correspond to the time-averaged electron pressure obtained from the GBS simulations on the target. (*b*) Time-averaged electron plasma pressure on the top of the simulation box, as obtained from the GBS non-linear simulation in steady-state.
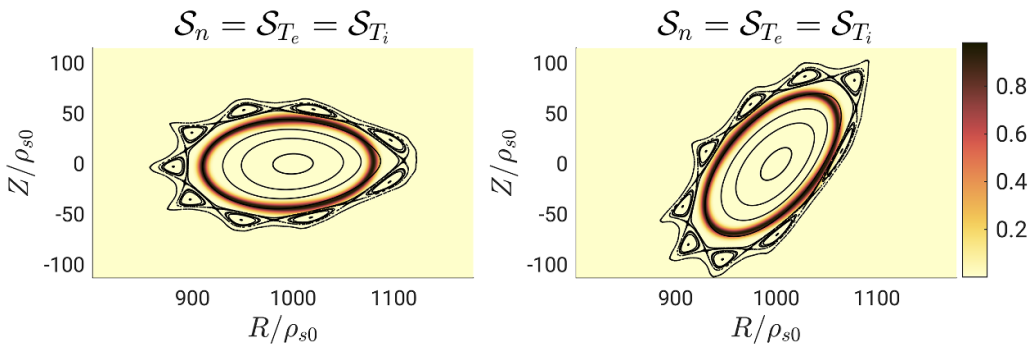

Figure 7. Density, electron temperature and ion temperature sources at two different poloidal planes.

The second term in equation (16) corresponds to the $\mathbf{E} \times \mathbf{B}$ flux, the third term to the electron diamagnetic flux, and the fourth term to the electron parallel flux. These terms are integrated over the plasma volume inside the LCFS, and the time evolution of the integral is shown in figure 8. The plot shows that the simulation reaches a quasi-steady state at $t \approx$
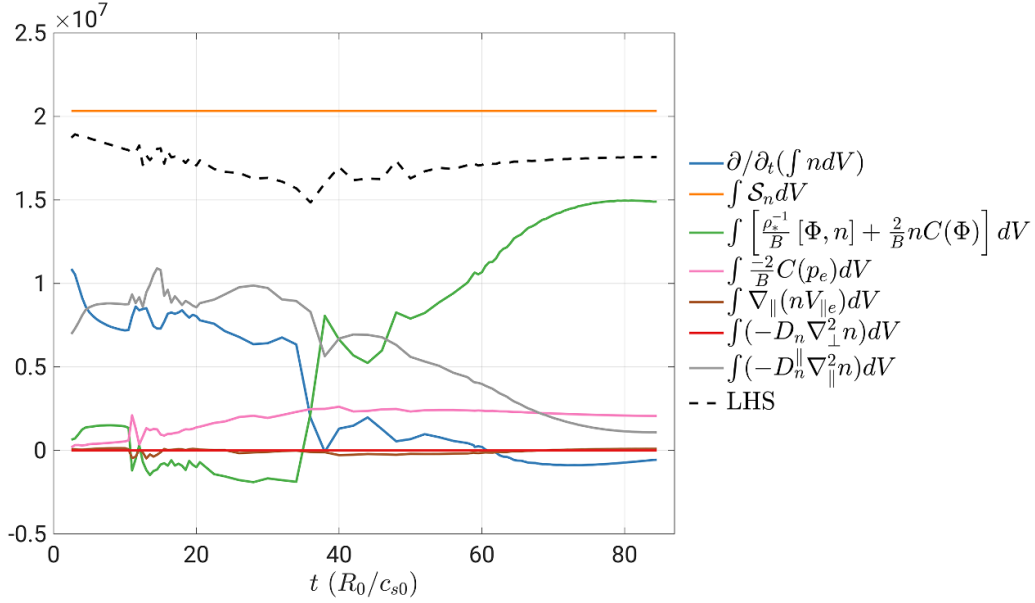
Figure 8. Volume integral of each term in the density equation. The system reaches a quasi-steady state at $t \approx 70 R_0/c_{s0}$. The mode $m = 4$ appears at $t \approx 35 R_0/c_{s0}$.
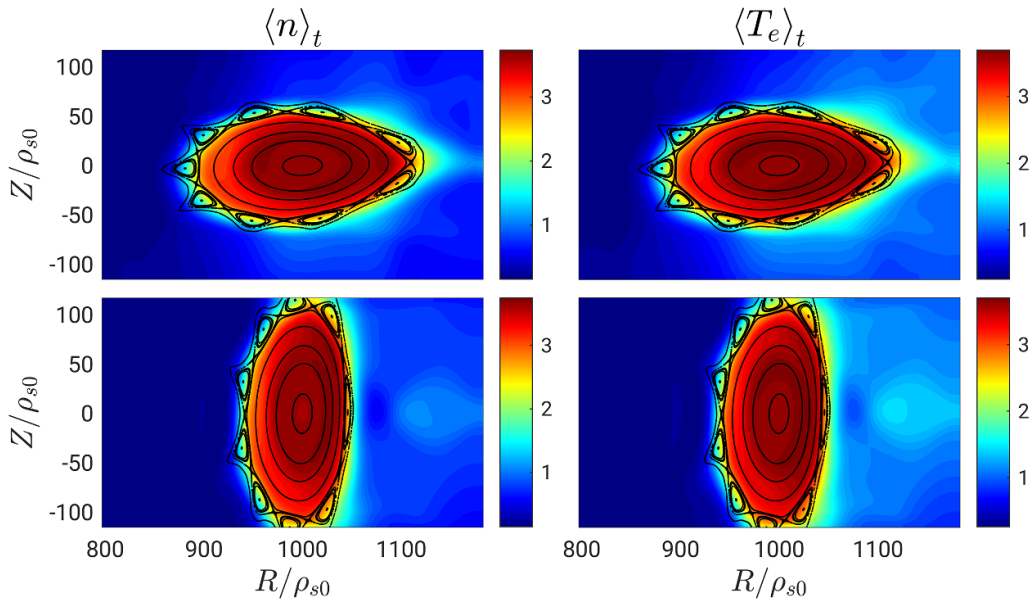

Figure 9. Equilibrium profiles of density (left) and electron temperature (right), obtained by time-averaging the simulation results. Top and bottom correspond to the toroidal planes $\phi = 0$ and $\phi = 0.6$, respectively.

$70 R_0/c_{s0}$, with the radial $\mathbf{E} \times \mathbf{B}$ flux dominating over the other fluxes. The sum of all terms on the left-hand side of (16) balances the source term within an error of 14%, reflecting the numerical error of the volume integration and the approximation used in evaluating the time derivative $\partial_t (\int n \mathrm{d}V)$. In fact, while time derivatives are discretized with a fourth-order Runge–Kutta scheme in GBS, we have used a second-order finite-differences scheme when computing the term $\partial_t (\int n \mathrm{d}V)$. This difference, along with the low sampling frequency of the data used to evaluate the quantities in figure 8, leads to errors of the order of 10%.

4.3. Equilibrium profiles

In figure 9 we show the equilibrium (time-averaged over the quasi-steady state) density and electron temperature profiles, which are very similar. Density and temperature peak in the center and decay radially across the flux surfaces, confirming that the prescribed configuration confines particles and heat within the LCFS. We note that the gradients are steeper at the HFS than at the LFS, which has consequences on the position of the peaks of the turbulent flux, as discussed in section 4.5. As expected, most of the particles and heat
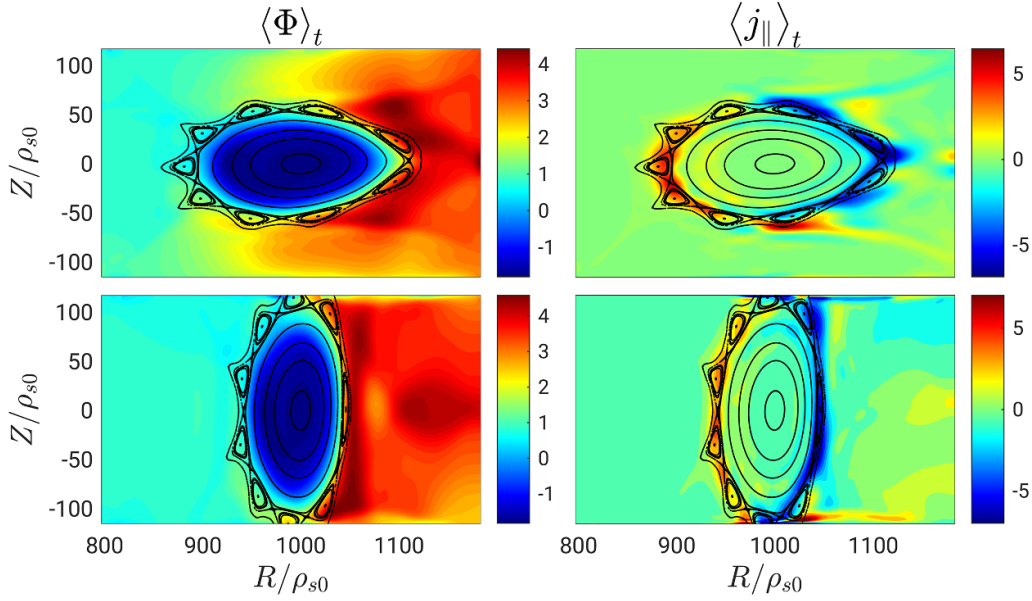
Figure 10. Equilibrium profiles of electrostatic potential (left) and parallel current (right), obtained by time-averaging the simulation results. Top and bottom correspond to the toroidal planes $\phi = 0$ and $\phi = 0.6$, respectively.

is deposited where the island magnetic field lines strike the top and bottom of the simulation domain. This is shown in figure 6(*b*), where the equilibrium electron pressure, $\langle p_e \rangle_t = \langle nT_e \rangle_t$, on the top of the simulation box is presented. The pressure peaks at the footprints of the island field-lines on the vessel.

In figure 10 we show the equilibrium profiles of the electrostatic potential and parallel current. $j_\parallel$ has a sinusoidal-like profile along the poloidal direction in the island region. In fact, $\langle \nabla \cdot \mathbf{j} \rangle_t = 0$ implies $|\nabla_\parallel j_\parallel| \sim |\nabla_\perp j_{dia}|$, and since $\mathbf{j}_{dia} = \nabla p \times \mathbf{B}/B^2$, the Pfirsch–Schlüter current modulation $j_\parallel \sim \cos(\theta)$ is expected from the $1/R$ nature of the magnetic field. We note that the potential profile in the core region is quite flat leading to an almost-zero radial electric field, E_r. In fact, in the core, where fluctuations have small amplitude, $\langle E_r \rangle_t \equiv -\partial_r \langle \Phi \rangle_t \sim \partial_r \langle p_i \rangle_t / \langle n \rangle_t$ (see derivation in [33]), as confirmed by figure 11 where this relation along R, at $\phi = 0$ and $Z = 0$, is shown to be satisfied in the core ($950\,\rho_{s0} \lesssim R \lesssim 1050\,\rho_{s0}$). Although not clear in the plot due to saturation of the colorbar scale, we note that strong parallel currents form at the magnetic presheath entrance in the region where the islands strike the simulation boundary, at the top and bottom walls. This is a result of the potential deviating substantially from ΛT_e at the top and bottom walls. We also note that a potentially-nonphysical negative potential is seen in the top boundary.

4.4. Nature of turbulent fluctuations

Snapshots of the density and potential fluctuations, evaluated as $\tilde{n} = n - \langle n \rangle_t$ and $\tilde{\Phi} = \Phi - \langle \Phi \rangle_t$, are shown in figure 12. A mode with toroidal mode number $n = 2$ and poloidal mode number $m = 4$ (corresponding to $k_y \rho_{s0} \approx 0.04$, where y is the
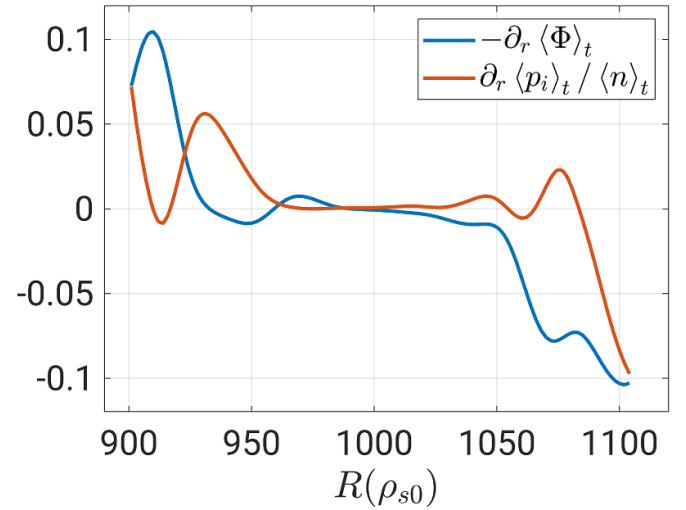

Figure 11. Comparison between equilibrium radial electric field, $-\partial_r \langle \Phi \rangle_t$, and pressure gradient, $\partial_r \langle p_i \rangle_t / \langle n \rangle_t$, along R at $\phi = 0$ and $Z = 0$.

binormal direction, while x and z are the radial and parallel coordinates) dominates the global dynamics of the system. The mode is coherent and rotates in the ion diamagnetic direction. We remark that the radial and poloidal wavenumbers of the mode are of the same order, $k_x \sim k_y$. This is in contrast with ballooning-driven tokamak edge turbulence, where $k_x \sim \sqrt{k_y/L_p}$ with L_p the equilibrium pressure length scale [34], meaning that $k_x < k_y$.

In figure 13 we display a snapshot of the potential fluctuations on the LCFS and its Fourier spectrum in straight-field-line coordinates (θ^*, ϕ), with θ^* defined such that $\frac{\mathbf{B} \cdot \nabla \theta^*}{\mathbf{B} \cdot \nabla \phi} = \iota$ is
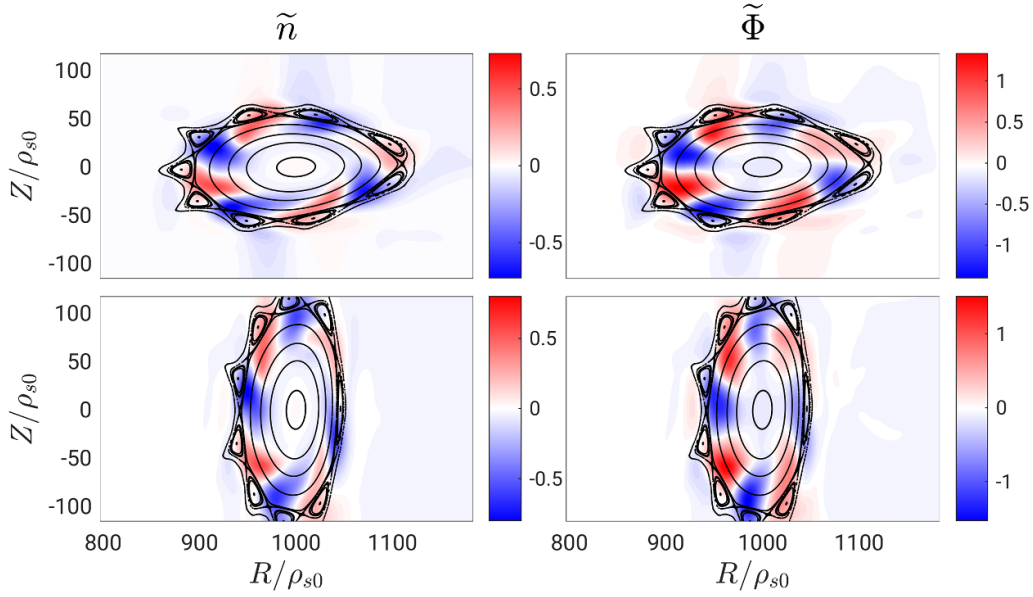
Figure 12. Snapshot of fluctuations of density (left) and electrostatic potential (right). Top and bottom correspond to the toroidal planes $\phi = 0$ and $\phi = 0.6$, respectively.
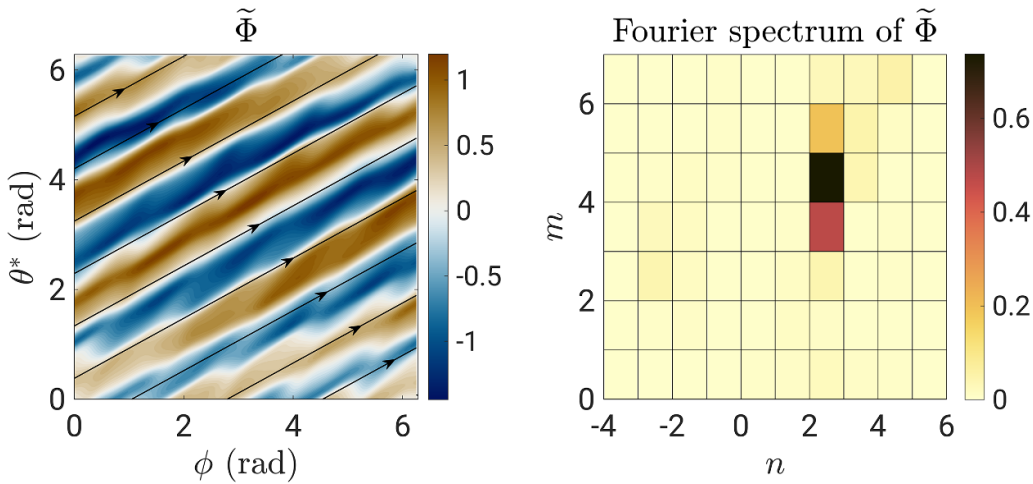

Figure 13. Snapshot of potential fluctuations on the LCFS (left) and its Fourier spectrum (right). The poloidal angle θ^* is such that field lines (black arrows) are straight in the (θ^*, ϕ) plane.

constant on a flux surface, showing that the dominant mode has $m = 4$ and $n = 2$ (Coelho *et al* [9] wrongly reports that the toroidal mode number is 5). Alongside the dominant mode, two sub-dominant modes corresponding to the side-bands $m = 3$ and $m = 5$ are present. We remark that the dominant and sub-dominant modes are global, i.e. they do not satisfy the 5-field periodicity of the stellarator. Such symmetry-breaking modes are reported to exist in the TJ-K stellarator experiment [11], as confirmed by GBS simulations of this machine. This underlines the importance of simulating the whole torus and not just one field-period.

We note that the dominant mode is field-aligned. Indeed, its poloidal and toroidal mode numbers are linked to the rotational transform through $\iota = n/m$. In fact, in a straight-field-line coordinate system (s, θ^*, ϕ), where s is a flux surface coordinate, the parallel gradient can be written as $\nabla_\parallel = \frac{B^\phi}{|B|} (\iota \partial_{\theta^*} + \partial_\phi)$, i.e. $k_\parallel = \frac{B^\phi}{|B|} (\iota m - n)$ in Fourier space, and therefore $k_\parallel \to 0$ implies $\iota = n/m$. In the current configuration, $\iota \approx 0.5$ throughout the whole volume, yielding $k_\parallel = 0$ for $n/m = 2/4$. In our previous Letter [9], we show, by means of a non-local linear theory, that the mode 2/4 is one of the few linear modes that can transport the $\mathbf{E} \times \mathbf{B}$ flux observed in the non-linear simulation. On the other hand, a simulation we performed with only one field-period shows a dominant mode with $n/m = 5/9$, a consequence of limiting the toroidal mode number to multiples of 5.
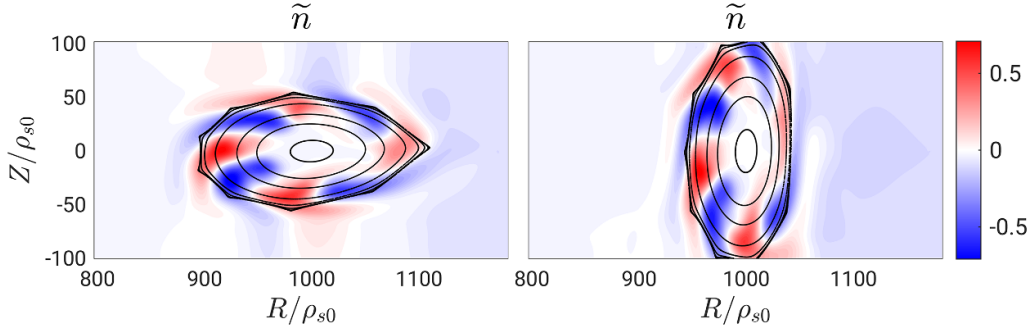
Figure 14. Snapshot of density fluctuations at two different planes in the configuration without islands.

A simulation with a configuration where the islands are removed (see figure 2) shows that the same dominant mode, $n/m = 2/4$, appears (see figure 14), leading us to conclude that the islands are not an important element in determining the properties of the dominant mode. Furthermore, the pressure profile is not flat inside the islands. Indeed, such flattening could only occur if the time-scale for the convection along the islands flux tubes, $\tau_\parallel$, is shorter than the rotation time-scale of the mode, τ_{mode}. Since the mode rotates with approximately the ion diamagnetic frequency, $\omega_{di} = v_{di}k_\perp$, where $v_{di} \sim c_s^2 T_e/(\Omega_i a)$ is the ion diamagnetic drift velocity, Ω_i the ion cyclotron frequency and a the plasma minor radius, and denoting L_c as the connection length of the island field lines, we have that

$$\frac{\tau_\parallel}{\tau_{\text{mode}}} \sim \frac{L_c/c_s}{\omega_{di}^{-1}} \sim \frac{L_c}{c_s}k_\perp v_{di} \sim \frac{L_c}{a}k_y\rho_s \gtrsim 1 \qquad (17)$$

since $L_c/a \gtrsim 100 R_0/a$ and $k_y\rho_s = 0.04$. This shows that convection along the island magnetic field lines occurs on a longer time-scale than the rotation of the mode, thus preventing the islands to all have the same flat pressure profile along them. This can be seen in the plots of the equilibrium density and temperature (figure 9).

Based on a reduced non-local linear theory, Coelho *et al* [9] points out the ballooning nature of the dominant mode [9]. In addition to this study, the nature of the mode can also be determined by comparing the amplitude of density fluctuations with those of the potential. Indeed, for resistive ballooning instabilities, $\nabla_\parallel \tilde{\Phi} \sim \nu \tilde{j}_\parallel$. From equation (4) this implies $\tilde{\Phi} \gg \tilde{n}$. In our simulation, the amplitude of the potential fluctuations is about twice as large as the amplitude of density fluctuations, as can be seen in figure 12. While this is not a conclusive observation that precludes the presence of other instabilities (drift-waves, for example), it is compatible with the previous statement on the ballooning nature of the dominant mode.

4.5. The turbulent **E** × **B** flux

The time-averaged **E** × **B** flux is characterized by the stellarator toroidal periodicity ($n = 5$). In fact, the instantaneous radial **E** × **B** flux (assuming **B** purely toroidal) is given by

$$\Gamma_{\text{E}\times\text{B}}^s = \frac{n}{B}\frac{\partial\Phi}{\partial\theta}\xi(s,\theta,\phi), \qquad (18)$$

in the coordinate system (s,θ,ϕ), where s is a flux surface label, and $\xi(s,\theta,\phi)$ is a geometrical factor such that in a stellarator has the same toroidal periodicity of the magnetic field and therefore can be written as $\xi(s,\theta,\phi) = \sum_{MN}|\xi_{MN}^s|e^{i(M\theta - NN_{\text{fp}}\phi)}$ (in the case of a tokamak with circular flux surfaces it reduces to $\xi = 1/r$). Since the density and potential fluctuations can be written as $n = \sum_{mn}|n_{mn}|e^{i(m\theta - n\phi + \omega t)}$ and $\Phi = \sum_{m'n'}|\Phi_{m'n'}|e^{i(m'\theta - n'\phi + \omega t - \Delta)}$, with Δ the phase difference between density and potential and ω the frequency of the mode, the time-averaged flux is

$$
\begin{aligned}
\langle\Gamma_{\text{E}\times\text{B}}^s\rangle_t &= \sum_{mn}\sum_{m'n'}\frac{m'|n_{mn}\Phi_{m'n'}|}{B}\sum_{MN}|\xi_{MN}^s| \\
&\quad \times \left\langle\Re\left(e^{i(m\theta - n\phi + \omega t)}\right)\Re\left(e^{i(m'\theta - n'\phi + \omega t - \Delta + \pi/2)}\right)\right. \\
&\quad \left.\times \Re\left(e^{i(M\theta - NN_{\text{fp}}\phi)}\right)\right\rangle_t \\
&= \sum_{mn}\sum_{m'n'}\frac{m'|n_{mn}\Phi_{m'n'}|}{B}\sum_{MN}|\xi_{MN}^s|\sin \\
&\quad \times [\Delta + (m-m')\theta - (n-n')\phi]\cos(M\theta - NN_{\text{fp}}\phi).
\end{aligned}
\qquad (19)
$$

The spectrum in figure 13 shows that all the dominant modes have $n = 2$ and thus equation (19) simplifies to

$$
\begin{aligned}
\langle\Gamma_{\text{E}\times\text{B}}^s\rangle_t &= \sum_m\sum_{m'}\frac{m'|n_{m2}\Phi_{m'2}|}{B}\sum_{MN}|\xi_{MN}^s|\sin \\
&\quad \times [\Delta + (m-m')\theta]\cos(M\theta - NN_{\text{fp}}\phi),
\end{aligned}
\qquad (20)
$$

showing that the toroidal periodicity of the time-averaged flux is dictated by the toroidal periodicity of the geometrical factor (which is a multiple of the field period). On the other hand, the poloidal dependence is an intricate convolution between the poloidal dependencies of the geometrical factor and the density and potential fluctuations.

As seen in figure 15, the flux peaks on the HFS rather than on the LFS, in contrast to typical observations in tokamaks.
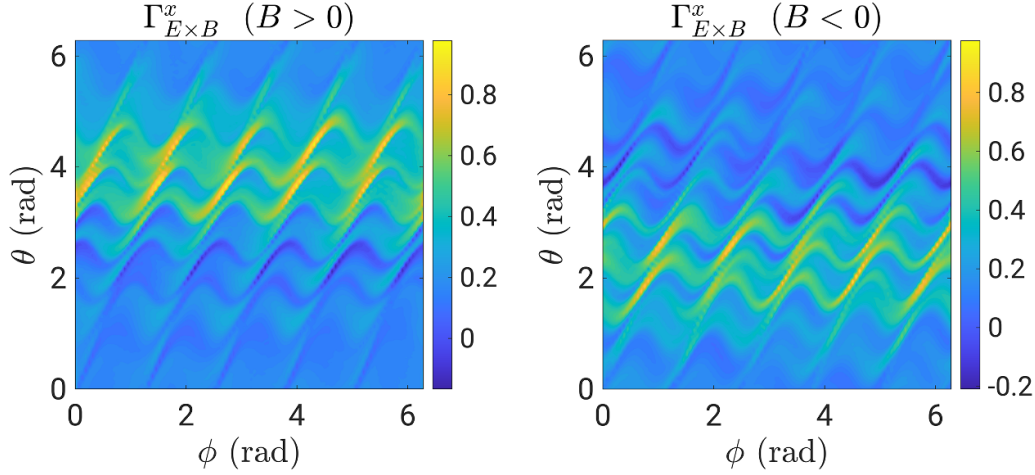
Figure 15. Time-averaged radial $\mathbf{E} \times \mathbf{B}$ flux on the LCFS for *positive* (left) and *negative* (right) magnetic field.

In the case $B_\phi > 0$ the peaks are localized around $\theta = 3\pi/2$, while in the $B_\phi < 0$ case around $\theta = \pi/2$.

We argue that the shift of the peak of the flux along the poloidal angle is a result of the poloidal dependence of the linear instabilities, as well as their convection due to an equilibrium $\mathbf{E} \times \mathbf{B}$ drift. We consider a reduced model of equations (1)–(7) that includes the main elements of the ballooning instability [35]:

$$
\begin{aligned}
\frac{\partial n}{\partial t} &= -\frac{\rho_*^{-1}}{B}[\Phi, n] \\
\frac{\partial T_e}{\partial t} &= -\frac{\rho_*^{-1}}{B}[\Phi, T_e] \\
\frac{\partial V_{\|e}}{\partial t} &= -\nu\left(\frac{m_i}{m_e}\right)nV_{\|e} + \left(\frac{m_i}{m_e}\right)\nabla_\| \Phi \\
\frac{\partial \nabla_\perp^2 \Phi}{\partial t} &= -\frac{B^2}{n}\nabla_\|\left(nV_{\|e}\right) + \frac{2B}{n}C(p_e).
\end{aligned}
\tag{21}
$$

We linearize the model by assuming that the density can be written as $n = n_0(x,z) + n_1(x,z)e^{ik_y y + \gamma t}$, where x is a local coordinate normal to the flux surface, z a coordinate along the magnetic field line and y the local binormal coordinate; n_0 is the background and n_1 the perturbation ($n_1 \ll n_0$). A similar expression is used for T_e, while for the potential and the electron parallel velocity we assume $\Phi_0 = 0$ and $V_{\|e0} = 0$. We retain the z dependence of the equilibrium density and electron temperature because the gradients depend on the poloidal angle (they are typically steeper on the HFS). In addition, we retain the x dependence of n_1 (and others), since we observe in the non-linear simulation $\partial_x n_1 \sim k_y n_1$. This contrasts with previous local linear theories of the drift-reduced Braginskii equations, where variations along the x direction are neglected, i.e. $k_x \ll k_y$ is assumed [35–37]. The present linearization leads to the following set of equations whose derivation is detailed in appendix B:

$$
\begin{aligned}
\gamma n_1 &= \mathtt{sign}(B_\phi)\rho_*^{-1}ik_y\frac{\partial n_0}{\partial x}\Phi_1 \\
\gamma T_{e1} &= \mathtt{sign}(B_\phi)\rho_*^{-1}ik_y\frac{\partial T_{e0}}{\partial x}\Phi_1 \\
\gamma V_{\|e1} &= -\nu\frac{m_i}{m_e}n_0 V_{\|e1} + \frac{m_i}{m_e}\frac{\partial}{\partial z}\Phi_1 \\
\gamma\nabla_\perp^2 \Phi_1 &= -\frac{\partial}{\partial z}V_{\|e1} + 2\left(\kappa_g\frac{\partial}{\partial x} + i\kappa_n k_y\right)T_{e1} \\
&\quad + 2\frac{T_{e0}}{n_0}\left(\kappa_g\frac{\partial}{\partial x} + i\kappa_n k_y\right)n_1,
\end{aligned}
\tag{22}
$$

where $\nabla_\perp^2 = \partial_x^2 - k_y^2 \equiv -k_\perp^2$, and κ_n and κ_g are the normalized normal and geodesic field-line curvatures, i.e. the projection of the curvature vector $\boldsymbol{\kappa} = -\mathbf{b} \times [\nabla \times \mathbf{b}]$ along the normal and binormal directions (normalized to R_0). Note that, when the field is reversed, κ_g changes sign while κ_n is not affected. By Fourier transforming the parallel and radial directions, $\partial/\partial z \to ik_\|$ and $\partial/\partial x \to ik_x$, a quadratic equation for the growth-rate is obtained:

$$
\gamma^2 + \frac{1}{\nu n_0}\left(\frac{k_\|}{k_\perp}\right)^2\gamma = 2\rho_*^{-1}\frac{k_y^2}{k_\perp^2}\left(\frac{T_{e0}}{n_0}\frac{\partial n_0}{\partial x} + \frac{\partial T_{e0}}{\partial x}\right)
$$
$$
\times\left(\mathtt{sign}(B_\phi)\frac{k_x}{k_y}\kappa_g + \kappa_n\right). \tag{23}
$$

While the $k_\|$ term is stabilizing, the drive of the ballooning instability appears on the right-hand side of equation (23) and it results from the density and temperature equilibrium gradients and the normal and geodesic components of the curvature. Note that $\mathtt{sign}(B_\phi)$ cancels out since κ_g changes sign when the field is reversed. This means that the dispersion relation in equation (23) depends on the direction of the magnetic field only through the equilibrium profiles (which, in the non-linear simulation, are slightly different due to the different frequency with which data is saved).

In an infinite aspect-ratio tokamak where $k_x \ll k_y$, one deduces from equation (23) that $\gamma^2 \sim \cos(\theta)$, consistent with
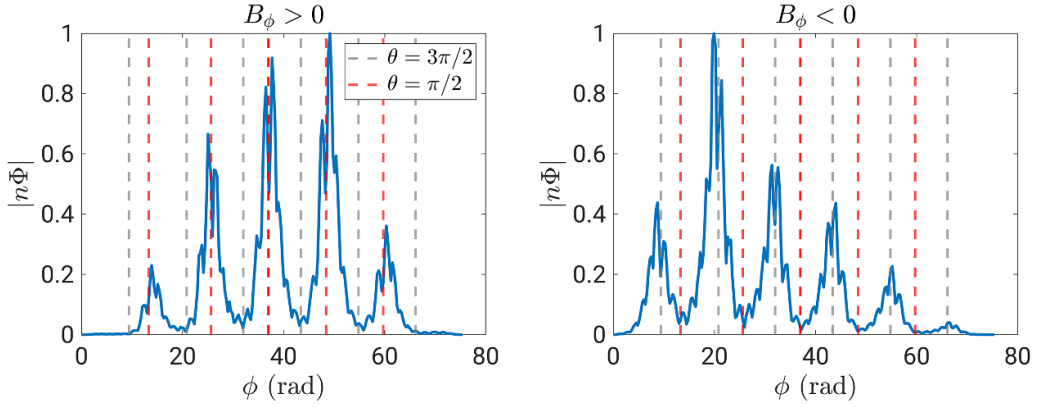
Figure 16. Product of the density and potential eigenmodes, $|n_1\Phi_1|$, for the forward and reversed magnetic field along the toroidal direction. The vertical dashed lines corresponds to the positions $\theta = \pi/2$ (red) and $\theta = 3\pi/2$ (grey). These are the eigenmodes that correspond to the eigenvalue with largest real part. In both cases, $\gamma \approx 3$.
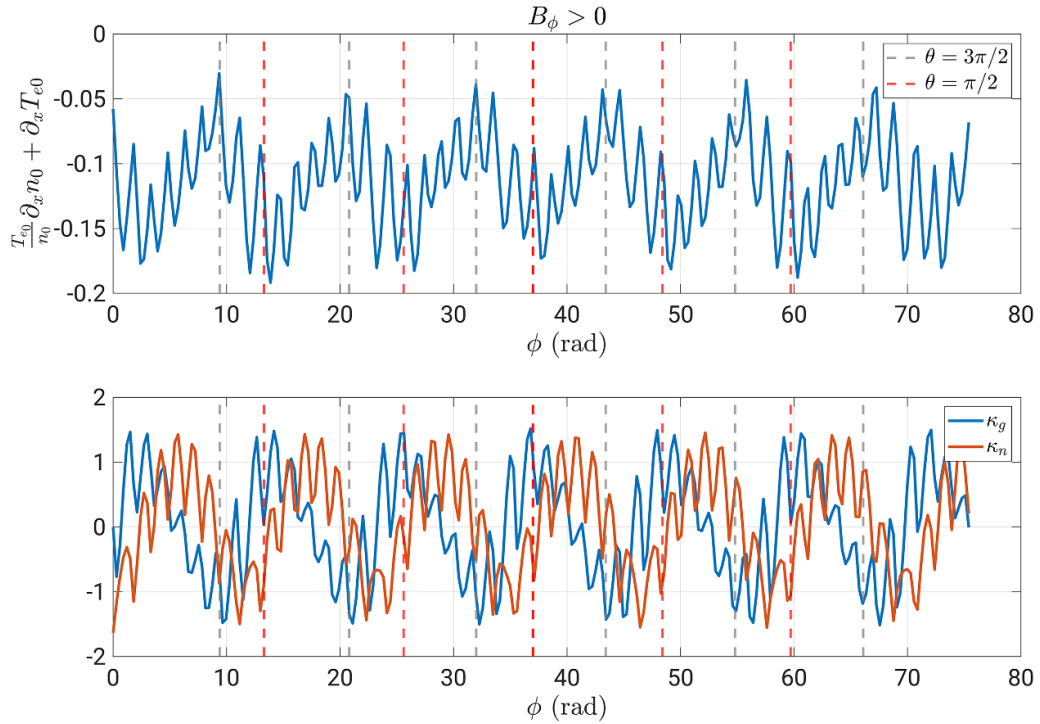

Figure 17. Equilibrium gradients, retrieved from the non-linear GBS simulation (top) and the normal and geodesic curvatures (bottom) used in the model in equation (22).

the common observation that turbulence is more developed at the LFS ($\theta \approx 0$) than at the HFS ($\theta \approx \pi$). On the other hand, the geodesic curvature is important when $k_x \sim k_y$, as it is observed in our non-linear simulations, thereby influencing the position of the eigenmodes maximum amplitude.

The solution of the 2D eigenvalue problem in equation (22), namely the product of the eigenmodes $|n_1\Phi_1|$ at the radial position where the density gradient has its maximum, is shown in figure 16 for $k_y\rho_{s0} = 0.04$, considering $B_\phi > 0$ and $B_\phi < 0$. The eigenmodes peak at $\theta = \pi/2$ and $\theta = 3\pi/2$, respectively, where the normal curvature is negative (but not where it has its minimum value) and the geodesic curvature is positive, as seen in figure 17 for the case $B_\phi > 0$ (the same applies for $B_\phi < 0$).

The peak position of the eigenmodes differ from the peak positions of the $\mathbf{E} \times \mathbf{B}$ flux observed in the non-linear simulation. In fact, the turbulent fluctuations are transported along the poloidal direction by the equilibrium $\mathbf{E} \times \mathbf{B}$ drift, $\langle \mathbf{V}_{\mathrm{E}\times\mathrm{B}} \rangle_t$, which is predominantly in the poloidal direction as shown in figure 18. The distance travelled by a turbulent eddy within the instability time-scale, $V^\theta_{\mathrm{E}\times\mathrm{B}}/\gamma$, is of the order of $\pi l/2$, with l the arc length of the LCFS in a single toroidal cross-section, in both the forward and reversed cases.

We draw the attention to the fact that the relevance of the geodesic curvature is pointed out to explain observations B.8.1)in the TJ-K stellarator. Experiments in this machine systematically observe the peak of the level of the density
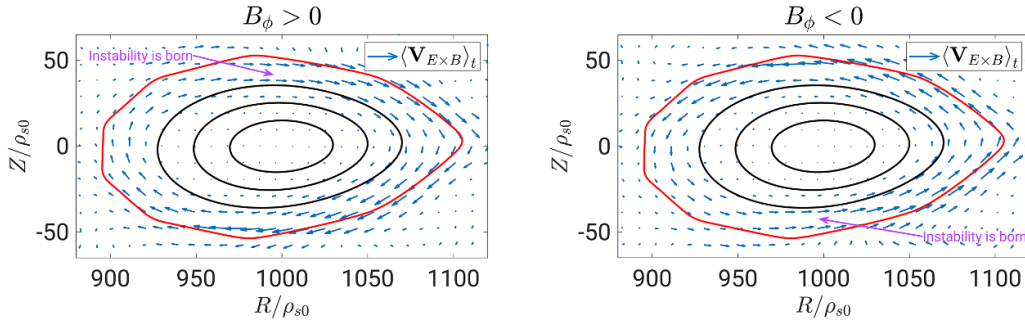
Figure 18. Equilibrium $\mathbf{E} \times \mathbf{B}$ drift, $\langle \mathbf{V}_{\mathrm{ExB}} \rangle_t$, in the forward and reversed field simulations.

and potential fluctuations where κ_n is negative and κ_g is positive [38, 39]. In the experiment, however, this region also coincides with the peaking of the $\mathbf{E} \times \mathbf{B}$ flux, whereas in our simulation the effect of the poloidal $\langle \mathbf{V}_{\mathrm{E} \times \mathrm{B}} \rangle_t$ convection is important.

5. Conclusions

The present paper describes the non-axisymmetric version of the GBS code, recently extended to handle three-dimensional magnetic configurations [9]. Using the expansion parameters δ, σ and Δ, the geometrical operators appearing in the drift-reduced Braginskii equations solved by GBS are expanded up to leading order, resulting in a perpendicular Laplacian that acts on the poloidal *RZ* plane and Poisson brackets that can still be numerically implemented using the Arakawa algorithm. This makes GBS implementation of the three-dimensional configurations similar to the axisymmetric version of the code.

We use the Dommaschk potentials to generate two vacuum magnetic fields, namely a configuration where a chain of islands surrounds the closed flux region mimicking an island divertor stellarator, and a configuration where the islands are replaced by a chaotic region, yielding a limited stellarator configuration. With the parameters of our simulations, we observe that the presence of the islands has a minor impact on the turbulent dynamics of the plasma.

The identification of the nature of the dominant mode as a ballooning-driven instability, based on a simplified non-local linear theory [9], is supported here by noticing that the amplitude of the potential fluctuations is larger than that of the density. The mode is field-aligned, $k_{\parallel} \to 0$, and its toroidal and poloidal mode numbers obey $\iota = n/m$ since $\iota = 0.5$ and $(n,m) = (2,4)$. We note that the dominant mode does not have the toroidal periodicity of the magnetic field. Symmetry-breaking modes are reported in the TJ-K stellarator experiment [11]. This observation in experiments, and now in simulations, underscores the importance of simulating the whole torus and not just one field-period.

When the magnetic field is reversed, $\mathbf{B} \to -\mathbf{B}$, the $\mathbf{E} \times \mathbf{B}$ flux peaks around $\theta = \pi/2$, in contrast to the $B_{\phi} > 0$ case where it peaks around $\theta = 3\pi/2$. A two-dimensional linear theory suggests that the instabilities develop at $\theta = \pi/2$ when $B_{\phi} > 0$, and at $\theta = 3\pi/2$ when $B_{\phi} < 0$ because the equilibrium gradients are poloidally asymmetric and tend to peak at

the HFS and the radial and poloidal elongations of the mode are similar, $k_x \sim k_y$. In these conditions, not only the normal curvature plays an important role, but also the geodesic one, effectively shifting the most destabilizing region away from $\theta = 0$. The mode is then transported in the poloidal direction by the equilibrium $\mathbf{E} \times \mathbf{B}$ drift, providing a possible explanation for the location of the peak of the turbulent flux.

One of the surprising outcomes of the simulations presented here is that the mode driving transport occurs on a large scale, it is coherent and has $k_x \sim k_y$. This is not the case in typical tokamak simulations and it is a subject currently under investigation. Preliminary results indicate that this difference is due to the small value of the magnetic shear and the ellipticity of the flux surfaces.

A natural next step in the study of island divertor configurations is the simulation of W7-AS and W7-X configurations. Although W7-AS is no longer operating, there is a large body of literature reporting on experimental measurements in different configurations [40], which can help with further validation of the GBS code. Moreover, the simulation of W7-AS constitutes a step forward towards the simulation of W7-X, a machine that shares many features with its predecessor but whose size is still prohibitively large for simulation purposes at the moment, in particular because of the time necessary to solve the Poisson equation for the electrostatic potential, the bottleneck of GBS [14]. Furthermore, we believe that the role of the neutrals cannot be neglected if one is interested in simulating meaningful scenarios in such large machines. This is the reason why a kinetic neutrals model, currently implemented in the tokamak version of the code [41], is being ported to the stellarator version of GBS.

Acknowledgments

Appendix A. Expansion of the geometrical operators

The parallel gradient, Poisson brackets and curvature operators can be written in cylindrical coordinates as follows:

$$\nabla_{\parallel} u = \frac{B_R}{B} \frac{\partial u}{\partial R} + \frac{B_\phi}{B} \frac{1}{R} \frac{\partial u}{\partial \phi} + \frac{B_Z}{B} \frac{\partial u}{\partial Z}, \qquad (A.1)$$

$$[\Phi, u] = \frac{B_R}{B} \left[\frac{1}{R} \frac{\partial \Phi}{\partial \phi} \frac{\partial u}{\partial Z} - \frac{\partial \Phi}{\partial Z} \frac{1}{R} \frac{\partial u}{\partial \phi} \right] + \frac{B_\phi}{B} \left[\frac{\partial \Phi}{\partial Z} \frac{\partial u}{\partial R} - \frac{\partial \Phi}{\partial R} \frac{\partial u}{\partial Z} \right]$$
$$+ \frac{B_Z}{B} \left[\frac{\partial \Phi}{\partial R} \frac{1}{R} \frac{\partial u}{\partial \phi} - \frac{1}{R} \frac{\partial \Phi}{\partial \phi} \frac{\partial u}{\partial R} \right], \qquad (A.2)$$

$$C(u) = C_R \frac{\partial u}{\partial R} + C_\phi \frac{1}{R} \frac{\partial u}{\partial \phi} + C_Z \frac{\partial u}{\partial Z}, \qquad (A.3)$$

where the coefficients C_R, C_ϕ, C_Z are given by

$$C_R = -\frac{B_Z}{B} \frac{1}{B} \frac{1}{R} \frac{\partial B}{\partial \phi} + \frac{B_\phi}{B} \frac{1}{B} \frac{\partial B}{\partial Z} + \frac{1}{2B} \left[\frac{1}{R} \frac{\partial B_Z}{\partial \phi} - \frac{\partial B_\phi}{\partial Z} \right], \qquad (A.4)$$

$$C_\phi = -\frac{B_R}{B} \frac{1}{B} \frac{\partial B}{\partial Z} + \frac{B_Z}{B} \frac{1}{B} \frac{\partial B}{\partial R} + \frac{1}{2B} \left[\frac{\partial B_R}{\partial Z} - \frac{\partial B_Z}{\partial R} \right], \quad (A.5)$$

$$C_Z = -\frac{B_\phi}{B} \frac{1}{B} \frac{\partial B}{\partial R} + \frac{B_R}{B} \frac{1}{B} \frac{1}{R} \frac{\partial B}{\partial \phi} + \frac{1}{2B} \left[\frac{1}{R} \frac{\partial (R B_\phi)}{\partial R} - \frac{1}{R} \frac{\partial B_R}{\partial \phi} \right]. \qquad (A.6)$$

The terms inside the square brackets vanish in the case of a vacuum magnetic field (where $\nabla \times \mathbf{B} = 0$). We now order these terms using the small parameters δ, σ and Δ defined in section 2. We first consider the scaling of the fields evolved by GBS, such as density and temperature, and then the scaling of the magnetic field.

The first-order derivatives of the quantities evolved by GBS scale as

$$\frac{\partial u}{\partial R} \sim \frac{u}{l_\perp}, \qquad \frac{\partial u}{\partial Z} \sim \frac{u}{l_\perp}, \qquad (A.7)$$

where $l_\perp$ is the perpendicular length scale of fluctuations. Indeed, since $u = \langle u \rangle_t + \widetilde{u}$, it follows $\partial_R u \sim \langle u \rangle_t / L_\perp + \widetilde{u}/l_\perp$, where $L_\perp$ is the equilibrium perpendicular length scale (the perpendicular plane coincides with the *RZ*-plane except for

an error of order δ). Because $L_\perp \sim a \gg \rho_{s0} \sim l_\perp$ and in the plasma boundary $\langle u \rangle_t \sim \widetilde{u}$, we can write $\partial_R u \sim u/l_\perp$. The same observation applies for the Z coordinate. In addition, we find that

$$\frac{1}{R} \frac{\partial u}{\partial \phi} \sim u \frac{\delta}{l_\perp}. \qquad (A.8)$$

In fact,

$$\frac{1}{R} \frac{\partial u}{\partial \phi} = \boldsymbol{e}_\phi \cdot \boldsymbol{\nabla} u = \boldsymbol{e}_\phi \cdot \left[(\nabla_{\parallel} u) \mathbf{b} + (\nabla_\perp u) \mathbf{e}_\perp \right]$$
$$= \underbrace{\frac{B_\phi}{B}}_{1+\mathcal{O}(\delta^2)} \underbrace{\nabla_{\parallel} u}_{u/l_{\parallel}} + \underbrace{(\nabla_\perp u)}_{u/l_\perp} \boldsymbol{e}_\phi \cdot \boldsymbol{e}_\perp, \qquad (A.9)$$

where $l_{\parallel}$ is the parallel length scale of fluctuations. Similarly to the perpendicular direction, we have $\nabla_{\parallel} u \sim \langle u \rangle_t / L_{\parallel} + \widetilde{u}/l_{\parallel}$, with $l_{\parallel} \sim R_0 \ll L_{\parallel}$. Therefore, $\nabla_{\parallel} u \sim u/l_{\parallel}$. Since $\boldsymbol{e}_\phi \cdot \boldsymbol{e}_\perp \sim \mathcal{O}(\delta)$, then

$$\frac{1}{R} \frac{\partial u}{\partial \phi} \sim \frac{u}{l_{\parallel}} \left(1 + \frac{l_{\parallel}}{l_\perp} \delta \right) \sim \frac{u}{l_{\parallel}} \left(1 + \sigma^{-1} \delta \right). \qquad (A.10)$$

Moreover, $\sigma \ll \delta$ in typical conditions, and

$$\frac{B_\phi}{B} = \frac{\pm \sqrt{B^2 - B_R^2 - B_Z^2}}{B} = \pm \sqrt{1 - 2\delta^2} = \pm 1 + \mathcal{O}\left(\delta^2\right), \qquad (A.11)$$

which yields the result in equation (A.8).

Due to the periodicity of the field, we can write $\partial_\phi B_R \sim m B_R$ and $\partial_\phi B_Z \sim m B_Z$, where m is the highest toroidal mode number of the magnetic field, which is a multiple of the field period.

The parameter Δ allows us to write $\partial_\phi B / B \sim m\Delta$. By introducing the radius a of the LCFS, we can write

$$\frac{\partial B_R}{\partial R} \sim \frac{\partial B_R}{\partial Z} \sim \frac{B_R}{a}, \qquad \frac{\partial B_Z}{\partial R} \sim \frac{\partial B_Z}{\partial Z} \sim \frac{B_Z}{a}. \qquad (A.12)$$

Using the vacuum condition $\partial_\phi B_Z / R = \partial_Z B_\phi$, we have that $\partial_Z B_\phi \sim m B_Z / R_0$, and we can finally write:

$$\frac{1}{B} \frac{\partial B}{\partial R} = \underbrace{\frac{B_R}{B} \frac{1}{B} \frac{\partial B_R}{\partial R}}_{\delta^2 \epsilon^{-1}/R_0} + \underbrace{\frac{B_\phi}{B} \frac{1}{B} \frac{\partial B_\phi}{\partial R}}_{1/R_0} + \underbrace{\frac{B_Z}{B} \frac{1}{B} \frac{\partial B_Z}{\partial R}}_{\delta^2 \epsilon^{-1}/R_0} \sim \frac{1}{R_0}, \quad (A.13)$$

$$\frac{1}{B} \frac{\partial B}{\partial Z} = \underbrace{\frac{B_R}{B} \frac{1}{B} \frac{\partial B_R}{\partial Z}}_{\delta^2 \epsilon^{-1}/R_0} + \underbrace{\frac{B_\phi}{B} \frac{1}{B} \frac{\partial B_\phi}{\partial Z}}_{m\delta/R_0} + \underbrace{\frac{B_Z}{B} \frac{1}{B} \frac{\partial B_Z}{\partial Z}}_{\delta^2 \epsilon^{-1}/R_0} \sim \frac{m\delta}{R_0}. \quad (A.14)$$

We retain only the terms scaling with $1/R_0$ and $m\delta/R_0$ since they dominate over the other terms (as long as $\delta^2 \ll \epsilon$).

We now turn to the geometric operators. The physical length scales of the parallel gradient, Poisson brackets and curvature operators are $l_{\parallel}$, $l_\perp^2$ and $R_0 l_\perp$ respectively. Note, however, that we use R_0 and ρ_{s0} as normalization factors of GBS since $l_{\parallel}$ and $l_\perp$ cannot be determined *a priori*; they correspond to the turbulence length scales in the parallel and

perpendicular directions, and are a result of the simulations. Nonetheless, it is expected that $l_\parallel \sim R_0$ and $\rho_{s0} \lesssim l_\perp \ll R_0$.

For the parallel gradient, we have

$$l_\parallel \nabla_\parallel u = \underbrace{l_\parallel \frac{B_R}{B} \frac{\partial u}{\partial R}}_{\delta \sigma^{-1}} + \underbrace{l_\parallel \frac{B_\phi}{B} \frac{1}{R} \frac{\partial u}{\partial \phi}}_{\delta \sigma^{-1}} + \underbrace{l_\parallel \frac{B_Z}{B} \frac{\partial u}{\partial Z}}_{\delta \sigma^{-1}}, \qquad (A.15)$$

where all terms are order 1 and cannot be neglected. Similarly, for the Poisson brackets we have

$$l_\perp^2 [\Phi, u]$$

$$= \underbrace{\frac{B_R}{B} l_\perp^2 \frac{1}{R} \frac{\partial \Phi}{\partial \phi} \frac{\partial u}{\partial Z}}_{\delta} - \underbrace{\frac{B_R}{B} l_\perp^2 \frac{\partial \Phi}{\partial Z} \frac{1}{R} \frac{\partial u}{\partial \phi}}_{\delta} + \underbrace{\frac{B_\phi}{B} l_\perp^2 \frac{\partial \Phi}{\partial Z} \frac{\partial u}{\partial R}}_{1}$$

$$- \underbrace{\frac{B_\phi}{B} l_\perp^2 \frac{\partial \Phi}{\partial R} \frac{\partial u}{\partial Z}}_{1} + \underbrace{\frac{B_Z}{B} l_\perp^2 \frac{\partial \Phi}{\partial R} \frac{1}{R} \frac{\partial u}{\partial \phi}}_{\delta} - \underbrace{\frac{B_Z}{B} l_\perp^2 \frac{1}{R} \frac{\partial \Phi}{\partial \phi} \frac{\partial u}{\partial R}}_{\delta},$$

$$(A.16)$$

where only the third and fourth terms are retained. Regarding the curvature operator in the vacuum limit,

$$l_\perp R_0 C_R \frac{\partial u}{\partial R} = - \underbrace{R_0 \frac{B_Z}{B} \frac{1}{R} \frac{1}{B} \frac{\partial B}{\partial \phi}}_{\delta m \Delta} \underbrace{l_\perp \frac{\partial u}{\partial R}}_{1} + \underbrace{R_0 \frac{B_\phi}{B} \frac{1}{B} \frac{\partial B}{\partial Z}}_{m\delta} \underbrace{l_\perp \frac{\partial u}{\partial R}}_{1} \qquad (A.17)$$

$$l_\perp R_0 C_\phi \frac{1}{R} \frac{\partial u}{\partial \phi} = - \underbrace{R_0 \frac{B_R}{B} \frac{1}{B} \frac{\partial B}{\partial Z}}_{\delta m \delta} \underbrace{l_\perp \frac{1}{R} \frac{\partial u}{\partial \phi}}_{\delta} + \underbrace{R_0 \frac{B_Z}{B} \frac{1}{B} \frac{\partial B}{\partial R}}_{\delta} \underbrace{l_\perp \frac{1}{R} \frac{\partial u}{\partial \phi}}_{\delta} \qquad (A.18)$$

$$l_\perp R_0 C_Z \frac{\partial u}{\partial Z} = - \underbrace{R_0 \frac{B_\phi}{B} \frac{1}{B} \frac{\partial B}{\partial R}}_{1} \underbrace{l_\perp \frac{\partial u}{\partial Z}}_{1} + \underbrace{R_0 \frac{B_R}{B} \frac{1}{R} \frac{1}{B} \frac{\partial B}{\partial \phi}}_{\delta m \Delta} \underbrace{l_\perp \frac{\partial u}{\partial Z}}_{1}, \qquad (A.19)$$

only the second term of (A.17) and the first term of (A.19) are retained. The same expansion can be applied to the parallel and perpendicular Laplacians, yielding equations (12) and (13).

Appendix B. Linearization of the drift-reduced Braginskii equations

We start by defining a field-aligned coordinate system (x, y, z), where x is a flux surface coordinate, z is the parallel coordinate and y a coordinate along the binormal direction. The orthogonal unit vectors are introduced,

$$e_1(z) = \frac{d\mathbf{r}_0}{dz} = \texttt{sign}(B_\phi) \mathbf{b}(z), \qquad (B.1.1)$$

$$e_2(z) = \widehat{\mathbf{n}}(z), \qquad (B.1.2)$$

$$e_3(z) = e_1 \times e_2, \qquad (B.1.3)$$

where $\mathbf{r}_0$ is the position of a given field line (depending only on the parallel coordinate), $\mathbf{b} = \mathbf{B}/B$ and $\widehat{\mathbf{n}}$ is the normal unit

vector to the flux surface, allow us to define the position $\mathbf{r}$ of any point around a given field line:

$$\mathbf{r} = \mathbf{r}_0(z) + x e_2(z) + y e_3(z) \qquad (B.2)$$

for x and y small (in the general case, e_2 and e_3 also depend on x and y). The covariant basis is formulated as:

$$\mathbf{e_x} = \frac{\partial \mathbf{r}}{\partial x} = e_2, \qquad (B.3.1)$$

$$\mathbf{e_y} = \frac{\partial \mathbf{r}}{\partial y} = e_3, \qquad (B.3.2)$$

$$\mathbf{e_z} = \frac{\partial \mathbf{r}}{\partial z} = e_1 + x \frac{\partial e_2}{\partial z} + y \frac{\partial e_3}{\partial z}. \qquad (B.3.3)$$

The covariant metric tensor is given by $g_{ij} = \mathbf{e_i} \cdot \mathbf{e_j}$:

$$g_{xx} = 1, \qquad (B.4.1)$$

$$g_{yy} = 1, \qquad (B.4.2)$$

$$g_{xy} = g_{yx} = 0, \qquad (B.4.3)$$

$$g_{xz} = x \underbrace{\frac{\partial e_2}{\partial z} \cdot e_2}_{0} + y \frac{\partial e_3}{\partial z} \cdot e_2 = g_{zx} \qquad (B.4.4)$$

$$g_{yz} = x \frac{\partial e_2}{\partial z} \cdot e_3 + y \underbrace{\frac{\partial e_3}{\partial z} \cdot e_3}_{0} = g_{zy} \qquad (B.4.5)$$

$$g_{zz} = 1 + 2x \frac{\partial e_2}{\partial z} \cdot e_1 + 2y \frac{\partial e_3}{\partial z} \cdot e_1 + 2xy \frac{\partial e_2}{\partial z} \cdot \frac{\partial e_3}{\partial z}$$

$$+ x^2 \left| \frac{\partial e_2}{\partial z} \right|^2 + y^2 \left| \frac{\partial e_3}{\partial z} \right|^2, \qquad (B.4.6)$$

$$g = \begin{pmatrix} 1 & 0 & g_{xz} \\ 0 & 1 & g_{yz} \\ g_{xz} & g_{yz} & g_{zz} \end{pmatrix} \qquad (B.5)$$

and the Jacobian by

$$\mathcal{J} = \sqrt{g_{zz} - g_{xz}^2 - g_{yz}^2}. \qquad (B.6)$$

The contravariant metric tensor $g^{ij} = \mathrm{Inv}(g_{ij})$ is

$$g^{xx} = \frac{g_{zz} - g_{yz}^2}{\mathcal{J}^2}, \qquad (B.7.1)$$

$$g^{yy} = \frac{g_{zz} - g_{xz}^2}{\mathcal{J}^2}, \qquad (B.7.2)$$

$$g^{xy} = \frac{g_{xz} g_{yz}}{\mathcal{J}^2} = g^{yx}, \qquad (B.7.3)$$

$$g^{xz} = -\frac{g_{xz}}{\mathcal{J}^2} = g^{zx} \qquad (B.7.4)$$

$$g^{yz} = -\frac{g_{yz}}{\mathcal{J}^2} = g^{zy} \qquad (B.7.5)$$

$$g^{zz} = \frac{1}{\mathcal{J}^2}, \qquad (B.7.6)$$

and the contravariant basis $\nabla i = g^{ij}\mathbf{e_j}$ is:

$$\nabla x = g^{xx}\mathbf{e_x} + g^{xy}\mathbf{e_y} + g^{xz}\mathbf{e_z} \tag{B.8.1}$$

$$= g^{xx}\boldsymbol{e_2} + g^{xy}\boldsymbol{e_3} + g^{xz}\left[\boldsymbol{e_1} + x\frac{\partial \boldsymbol{e_2}}{\partial z} + y\frac{\partial \boldsymbol{e_3}}{\partial z}\right], \tag{B.8.2}$$

$$\nabla y = g^{yx}\mathbf{e_x} + g^{yy}\mathbf{e_y} + g^{yz}\mathbf{e_z} \tag{B.8.3}$$

$$= g^{yx}\boldsymbol{e_2} + g^{yy}\boldsymbol{e_3} + g^{yz}\left[\boldsymbol{e_1} + x\frac{\partial \boldsymbol{e_2}}{\partial z} + y\frac{\partial \boldsymbol{e_3}}{\partial z}\right], \tag{B.8.4}$$

$$\nabla z = g^{zx}\mathbf{e_x} + g^{zy}\mathbf{e_y} + g^{zz}\mathbf{e_z} \tag{B.8.5}$$

$$= g^{zx}\boldsymbol{e_2} + g^{zy}\boldsymbol{e_3} + g^{zz}\left[\boldsymbol{e_1} + x\frac{\partial \boldsymbol{e_2}}{\partial z} + y\frac{\partial \boldsymbol{e_3}}{\partial z}\right]. \tag{B.8.6}$$

Note that $g(x=0,y=0) = g^{-1}(x=0,y=0)$ are equal to the 3×3 identity matrix.

We can now express the parallel gradient

$$\nabla_{\|}f = \mathbf{b} \cdot \nabla f = \boldsymbol{e_1} \cdot \left[\frac{\partial f}{\partial x}\nabla x + \frac{\partial f}{\partial y}\nabla y + \frac{\partial f}{\partial z}\nabla z\right], \tag{B.9}$$

and thus

$$\nabla_{\|}f\Big|_{\substack{y=0 \\ x=0}} = \frac{\partial f}{\partial z}. \tag{B.10}$$

As usual, we normalize the parallel gradient by R_0:

$$\nabla_{\|}f \to R_0\nabla_{\|}f = R_0\frac{\partial f}{\partial z}. \tag{B.11}$$

Since we are interested in discretizing the toroidal direction rather than the z direction, we make use of the following property:

$$z(\phi) = \int \left|\frac{B}{B_\phi}\right| R(\phi)\,d\phi \implies \frac{dz}{d\phi} = \left|\frac{B}{B_\phi}\right| R(\phi), \tag{B.12}$$

allowing us to write the normalized operator as

$$\nabla_{\|}f = R_0\left(\frac{\partial z}{\partial \phi}\right)^{-1}\frac{\partial f}{\partial \phi} = \left|\frac{B_\phi}{B}\right|\frac{R_0}{R}\frac{\partial f}{\partial \phi}. \tag{B.13}$$

Regarding the Poisson Brackets,

$$[\phi,f] = \mathbf{b} \cdot (\nabla\phi \times \nabla f) = \texttt{sign}(B_\phi)\boldsymbol{e_1} \cdot (\nabla\phi \times \nabla f). \tag{B.14}$$

Since

$$\nabla\phi \times \nabla f = \frac{1}{\mathcal{J}}\left[\left(\frac{\partial\phi}{\partial y}\frac{\partial f}{\partial z} - \frac{\partial\phi}{\partial z}\frac{\partial f}{\partial y}\right)\mathbf{e_x} + \left(\frac{\partial\phi}{\partial z}\frac{\partial f}{\partial x} - \frac{\partial\phi}{\partial x}\frac{\partial f}{\partial z}\right)\right.$$
$$\left.\times\mathbf{e_y} + \left(\frac{\partial\phi}{\partial x}\frac{\partial f}{\partial y} - \frac{\partial\phi}{\partial y}\frac{\partial f}{\partial x}\right)\mathbf{e_z}\right], \tag{B.15}$$

then

$$[\phi,f]\Big|_{\substack{y=0 \\ x=0}} = \texttt{sign}(B_\phi)\left(\frac{\partial\phi}{\partial x}\frac{\partial f}{\partial y} - \frac{\partial\phi}{\partial y}\frac{\partial f}{\partial x}\right). \tag{B.16}$$

We normalize the Poisson Brackets by ρ_{s0}^2:

$$[\phi,f] \to \rho_{s0}^2[\phi,f] = \texttt{sign}(B_\phi)\rho_{s0}^2\left(\frac{\partial\phi}{\partial x}\frac{\partial f}{\partial y} - \frac{\partial\phi}{\partial y}\frac{\partial f}{\partial x}\right)$$
$$= \texttt{sign}(B_\phi)\left(\frac{\partial\phi}{\partial(x/\rho_{s0})}\frac{\partial f}{\partial(y/\rho_{s0})}\right.$$
$$\left. - \frac{\partial\phi}{\partial(y/\rho_{s0})}\frac{\partial f}{\partial(x/\rho_{s0})}\right), \tag{B.17}$$

and we renormalize $x/\rho_{s0} \to x$ and $y/\rho_{s0} \to y$.

We now consider the curvature operator,

$$C(f) = \frac{B}{2}\left[\boldsymbol{\nabla} \times \frac{\boldsymbol{b}}{B}\right] \cdot \boldsymbol{\nabla}f = [\mathbf{b} \times \boldsymbol{\kappa}] \cdot \boldsymbol{\nabla}f, \tag{B.18}$$

where $\boldsymbol{\kappa} = -\mathbf{b} \times [\nabla \times \mathbf{b}]$ is the magnetic field-line curvature. By writing $\boldsymbol{\kappa} = \kappa_n\boldsymbol{e_2} + \kappa_g[\boldsymbol{e_2} \times \boldsymbol{e_1}] = \kappa_n\boldsymbol{e_2} - \kappa_g\boldsymbol{e_3}$, it follows that $[\mathbf{b} \times \boldsymbol{\kappa}] = \kappa_n\mathbf{e_y} + \kappa_g\mathbf{e_x}$, and thus

$$C(f)\Big|_{\substack{y=0 \\ x=0}} = \kappa_n\frac{\partial f}{\partial y} + \kappa_g\frac{\partial f}{\partial x}. \tag{B.19}$$

The operator is normalized by $R_0\rho_{s0}$:

$$C(f) \to R_0\rho_{s0}C(f) = R_0\kappa_n\frac{\partial f}{\partial(y/\rho_{s0})} + R_0\kappa_g\frac{\partial f}{\partial(x/\rho_{s0})}$$
$$\equiv \kappa_n\frac{\partial f}{\partial y} + \kappa_g\frac{\partial f}{\partial x}, \tag{B.20}$$

where $x/\rho_{s0} \to x$, $y/\rho_{s0} \to y$, $R_0\kappa_n \to \kappa_n$, and $R_0\kappa_g \to \kappa_g$. Note that κ_n does not change sign when the field is reversed, but κ_g does. Finally, the perpendicular Laplacian can be expressed as

$$\nabla_{\perp}^2 f = \nabla \cdot [(\mathbf{b} \times \nabla f) \times \mathbf{b}] = \nabla \cdot \left[\underbrace{(\boldsymbol{e_1} \times \nabla f) \times \boldsymbol{e_1}}_{\mathbf{G}}\right]. \tag{B.21}$$

Note that $\mathbf{G} = \hat{G}_2\boldsymbol{e_2} + \hat{G}_3\boldsymbol{e_3}$ since $\mathbf{G}$ is perpendicular to $\boldsymbol{e_1}$. We can further write $\mathbf{G} = \hat{G}_2\mathbf{e_x} + \hat{G}_3\mathbf{e_y}$ according to (B.3.1). This means that $\hat{G}_2$ and $\hat{G}_3$ are the contravariant components of $\mathbf{G}$. The perpendicular laplacian is evaluated according to

$$\nabla_{\perp}^2 f = \nabla \cdot \mathbf{G} = \frac{1}{\mathcal{J}}\sum_i\frac{\partial}{\partial q^i}\left(\mathcal{J}G^i\right) = \frac{1}{\mathcal{J}}\frac{\partial\mathcal{J}}{\partial x}G^2$$
$$+ \frac{1}{\mathcal{J}}\frac{\partial\mathcal{J}}{\partial y}G^3 + \frac{\partial G^2}{\partial x} + \frac{\partial G^3}{\partial y} \tag{B.22}$$
$$= \frac{1}{\mathcal{J}}\frac{\partial\mathcal{J}}{\partial x}\hat{G}_2 + \frac{1}{\mathcal{J}}\frac{\partial\mathcal{J}}{\partial y}\hat{G}_3 + \frac{\partial\hat{G}_2}{\partial x} + \frac{\partial\hat{G}_3}{\partial y}.$$

We obtain:

$$\nabla_{\perp}^2 f\Big|_{\substack{y=0 \\ x=0}} = \frac{\partial^2 f}{\partial x^2} + \frac{\partial^2 f}{\partial y^2} + \left(\frac{\partial\boldsymbol{e_2}}{\partial z}\cdot\boldsymbol{e_1}\right)\frac{\partial f}{\partial x} + \left(\frac{\partial\boldsymbol{e_3}}{\partial z}\cdot\boldsymbol{e_1}\right)\frac{\partial f}{\partial y}. \tag{B.23}$$
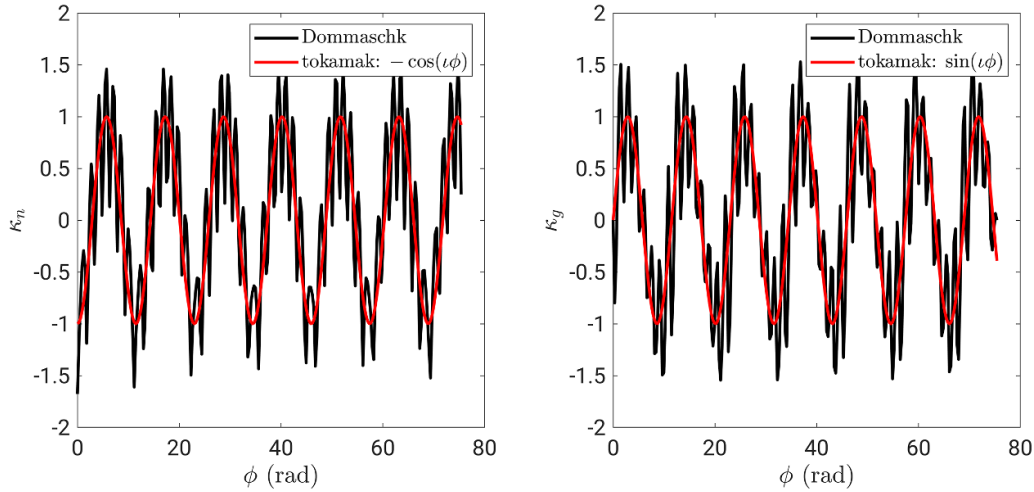
Figure B1. Normal, κ_n, and geodesic, κ_g, components of curvature $\boldsymbol{\kappa}$ along the field line that spans the LCFS of the Dommaschk equilibrium. For comparison, the curvatures of an infinite aspect-ratio tokamak with circular flux surfaces are shown in red, where $\iota = 0.547$.

The normalization is

$$\nabla_\perp^2 f \rightarrow \rho_{s0}^2 \nabla_\perp^2 f = \frac{\partial^2 f}{\partial x^2} + \frac{\partial^2 f}{\partial y^2} + \rho_{s0} \left(\frac{\partial \boldsymbol{e_2}}{\partial z} \cdot \boldsymbol{e_1} \right) \frac{\partial f}{\partial x}$$
$$+ \rho_{s0} \left(\frac{\partial \boldsymbol{e_3}}{\partial z} \cdot \boldsymbol{e_1} \right) \frac{\partial f}{\partial y}, \qquad \text{(B.24)}$$

meaning that the last two terms are R_0/ρ_{s0} times smaller than the first two and therefore we neglect them.

To derive a reduced set of equations able to describe the ballooning instability, we start from the model in equation (21). We assume that quantities vary as $f = f_0(x,z) + f_1(x,z)e^{ik_y y + \gamma t}$. For the potential and the electron parallel velocity we assume $f_0 = 0$. The z-dependence of the equilibrium density and electron temperature is retained because the gradients depend on the poloidal angle (they are typically steeper on the HFS). These assumptions lead to system in equation (22).

To numerically solve the system in equation (22), we recast it in matrix form, $\gamma \hat{A}\mathbf{x} = \hat{B}\mathbf{x}$. We define a two-dimensional regular grid, $x_i = x_0 + i\Delta x$ and $\phi = j\Delta\phi$ with $i = 0,\ldots,N_x - 1$ and $j = 0,\ldots,N_\phi - 1$. The operators ∂_z, ∂_x and ∂_x^2 are implemented with finite differences. We neglect the magnetic shear and assume infinite aspect-ratio, which allows us to set the grid spacing in the flux surface direction, Δx, to be the same at all z positions. This spacing is defined as the distance between the flux surfaces at the initial position where the field lines start to be followed (in our case we choose the starting position as $R = x_i$, $Z = 0$ and $\phi = 0$). Note that the equilibrium gradients, $\partial n_0/\partial x$ and $\partial T_{e0}/\partial x$, depend on x and ϕ and are computed from the non-linear simulations. The curvatures κ_n and κ_g depend on ϕ and very weakly on x. They are shown in figure B1 on the LCFS. For comparison, the reference values $\kappa_n = -\cos(\iota\phi)$ and $\kappa_g = \sin(\iota\phi)$ of an infinite aspect-ratio tokamak with circular flux surfaces are also shown.

ORCID iD

A.J. Coelho ⬤ https://orcid.org/0000-0002-8889-7259

References

[1] Pedersen T.S. *et al* 2022 Experimental confirmation of efficient island divertor operation and successful neoclassical transport optimization in Wendelstein 7-X *Nucl. Fusion* **62** 042022

[2] Beidler C.D. *et al* (the W7-X Team) 2021 Demonstration of reduced neoclassical energy transport in Wendelstein 7-X *Nature* **596** 221–6

[3] Maurer M., Bañón Navarro A., Dannert T., Restelli M., Hindenlang F., Görler T., Told D., Jarema D., Merlo G. and Jenko F. 2020 GENE-3D: a global gyrokinetic turbulence code for stellarators *J. Comput. Phys.* **420** 109694

[4] Cole M.D.J. , Hager R., Moritaka T., Dominski J., Kleiber R., Ku S., Lazerson S., Riemann J. and Chang C.S. 2019 Verification of the global gyrokinetic stellarator code XGC-S for linear ion temperature gradient driven modes *Phys. Plasmas* **26** 082501

[5] Barnes M., Parra F.I. and Landreman M. 2019 Stella: an operator-split, implicit-explicit delta f-gyrokinetic code for general magnetic field configurations *J. Comput. Phys.* **391** 365

[6] Sánchez E. , Mishchenko A., García-Regaña J.M., Kleiber R., Bottino A. and Villard L. 2020 Nonlinear gyrokinetic PIC simulations in stellarators with the code EUTERPE *J. Plasma Phys.* **86** 855860501

[7] Sánchez E. *et al* 2021 Gyrokinetic simulations in stellarators using different computational domains *Nucl. Fusion* **61** 116074

[8] Wilms F., Navarro A.B., Merlo G., Leppin L., Görler T., Dannert T., Hindenlang F. and Jenko F. 2021 Global electromagnetic turbulence simulations of W7-X-like plasmas with GENE-3D *J. Plasma Phys.* **87** 905870604

[9] Coelho A.J., Loizu J., Ricci P. and Giacomin M. 2022 Global fluid simulation of plasma turbulence in a stellarator with an island divertor *Nucl. Fusion* **62** 074004

[10] Shanahan B.W., Dudson B.D. and Hill P. 2019 Fluid simulations of plasma filaments in stellarator geometries with BSTING *Plasma Phys. Control. Fusion* **61** 025007

[11] Birkenmeier G. , Ramisch M., Fuchert G., Köhn A., Nold B. and Stroth U. 2013 Spatial structure of drift-wave turbulence and transport in a stellarator *Plasma Phys. Control. Fusion* **55** 015003

[12] Coelho A.J., Loizu J., Ricci P., Ramisch M., Köhn-Seemann A., Birkenmeier G. and Rahbarnia K. 2023

Validation of GBS plasma turbulence simulation of the TJ-K stellarator *Plasma Phys. Control. Fusion* **65** 085018

[13] Ricci P. , Halpern F.D., Jolliet S., Loizu J., Mosetto A., Fasoli A., Furno I. and Theiler C. 2012 Simulation of plasma turbulence in scrape-off layer conditions: the GBS code, simulation results and code validation *Plasma Phys. Control. Fusion* **54** 124047

[14] Giacomin M. , Ricci P., Coroado A., Fourestey G., Galassi D., Lanti E., Mancini D., Richart N., Stenger L.N. and Varini N. 2022 The GBS code for the self-consistent simulation of plasma turbulence and kinetic neutral dynamics in the tokamak boundary *J. Comput. Phys.* **464** 111294

[15] Halpern F.D. , Ricci P., Jolliet S., Loizu J., Morales J., Mosetto A., Musil F., Riva F., Tran T.M. and Wersal C. 2016 The GBS code for tokamak scrape-off layer simulations *J. Comput. Phys.* **315** 388

[16] Zeiler A. 1999 Tokamak edge turbulence *Max-Planck-Institut für Plasmaphysik* IPP 5/88

[17] Galassi D. *et al* 2022 Validation of edge turbulence codes in a magnetic X-point scenario in TORPEX *Phys. Plasmas* **29** 012501

[18] Giacomin M. and Ricci P. 2020 Investigation of turbulent transport regimes in the tokamak edge by using two-fluid simulations *J. Plasma Phys.* **86** 905860502

[19] Loizu J., Ricci P., Halpern F.D. and Jolliet S. 2012 Boundary conditions for plasma fluid models at the magnetic presheath entrance *Phys. Plasmas* **19** 122307

[20] Mosetto A., Halpern F.D., Jolliet S., Loizu J. and Ricci P. 2015 Finite ion-temperature effects on scrape-off layer turbulence *Phys. Plasmas* **22** 012308

[21] Boinnard T., Coelho A.J., Loizu J. and Ricci P. 2023 Plasma turbulence simulations in a diverted tokamak with applied resonant magnetic perturbations *Nucl. Fusion* **63** 076005

[22] Jolliet S., Halpern F.D., Loizu J., Mosetto A., Riva F. and Ricci P. 2015 Numerical approach to the parallel gradient operator in tokamak scrape-off layer turbulence simulations and application to the GBS code *Comput. Phys. Commun.* **188** 21–32

[23] Paruta P., Ricci P., Riva F., Wersal C., Beadle C. and Frei B. 2018 Simulation of plasma turbulence in the periphery of diverted tokamaks by using the GBS code *Phys. Plasmas* **26** 112301

[24] van Milligen B.P. and Lopez Fraguas A. 1994 Expansion of vacuum magnetic fields in toroidal harmonics *Comput. Phys. Commun.* **81** 74

[25] Miyamoto K. 1978 Recent stellarator research *Nucl. Fusion* **18** 243

[26] Dommaschk W. 1986 Representations for vacuum potentials in stellarators *Comput. Phys. Commun.* **40** 203

[27] Dommaschk W., Lotz W., and Nührenberg J. 1984 Detailed results of Monte Carlo simulation of neoclassical transport in stellarators *Max-Planck-Institut für Plasmaphysik*, IPP 0/48

[28] Dommaschk W. 1981 Solution to stellarator boundary value problems with set of simple toroidal harmonic functions *Z. Naturforsch.* A **36** 251

[29] Dewar R.L. and Hudson S.R. 1998 Stellarator symmetry *Physica* D **112** 275–80

[30] Helander P. 2014 Theory of plasma confinement in non-axisymmetric magnetic fields *Rep. Prog. Phys.* **77** 087001

[31] Loizu J., Hudson S.R., Nührenberg C., Geiger J. and Helander. P. 2017 Equilibrium β-limits in classical stellarators *J. Plasma Phys.* **83** 715830601

[32] Sinha P., Hölbe H., Pedersen T.S. and Bozhenkov S. (W7-X Team) 2017 Numerical studies of scrape-off layer connection length in Wendelstein 7-X *Nucl. Fusion* **58** 016027

[33] Giacomin M. 2022 Turbulent transport regimes in the tokamak boundary *PhD Thesis* EPFL

[34] Ricci P., Rogers B.N. and Brunner S. 2008 High- and low-confinement modes in simple magnetized toroidal plasmas *Phys. Rev. Lett.* **100** 225002

[35] Mosetto A., Halpern F., Jolliet S. and Ricci P. 2012 Low-frequency linear-mode regimes in the tokamak scrape-off layer *Phys. Plasmas* **19** 112103

[36] Riva F., Lanti E., Jolliet S. and Ricci P. 2017 Plasma shaping effects on tokamak scrape-off layer turbulence *Plasma Phys. Control. Fusion* **59** 035001

[37] Jolliet S., Halpern F.D., Loizu J., Mosetto A. and Ricci P. 2014 Aspect ratio effects on limited scrape-off layer plasma turbulence *Phys. Plasmas* **21** 022303

[38] Birkenmeier G. , Ramisch M., Manz P., Nold B. and Stroth U. 2011 Experimental investigation of the magnetic configuration dependence of turbulent transport *Phys. Rev. Lett.* **107** 255001

[39] Ramisch M., Birkenmeier G., Köhn A. and Stroth U. 2011 Linear drift-wave instability in TJ-K geometry *Proc. 38th EPS Conf. on Plasma Physics 2011* (*Strasbourg, France*) (available at: https://info.fusion.ciemat.es/OCS/eps2011pap/pdf/P5.111.pdf)

[40] Hirsch M. *et al* 2008 Major results from the stellarator Wendelstein 7-AS *Plasma Phys. Control. Fusion* **50** 053001

[41] Wersal C. and Ricci P. 2015 A first-principles self-consistent model of plasma turbulence and kinetic neutral dynamics in the tokamak scrape-off layer *Nucl. Fusion* **55** 123014